Scalable and Robust Multiband Modeling of AGN Light Curves in Rubin-LSST

```
Weixiang Yu (于伟翔) , John J. Ruan , Colin J. Burke , Roberto J. Assef , Tonima T. Ananna , Franz E. Bauer , Demetra De Cicco , Keith Horne , Lorena Hernández-García , 10,3,10,8,11 Dragana Ilić , Laudio , Andjelka B. Kovačević , Marcin Marculewicz , Savayamtrupta Panda , Laudio Ricci , Ananna , Sanchez-Sáez , Sarath Satheesh Sheeba , Francesco Tombesi , Andjelka B. Kovačević , Ananna , An
```

¹Department of Physics & Astronomy, Bishop's University, 2600 rue College, Sherbrooke, QC, J1M 1Z7, Canada
²Department of Astronomy, Yale University, 266 Whitney Avenue, New Haven, CT 06511, USA
³Instituto de Estudios Astrofísicos, Facultad de Ingenieríay Ciencias, Universidad Diego Portales, Av. Ejército Libertador 441, Santiago, Chile

⁴ Department of Physics and Astronomy, Wayne State University, 666 W. Hancock St, Detroit, MI, 48201, USA

⁵ Instituto de Alta Investigación, Universidad de Tarapacá, Casilla 7D, Arica, Chile

⁶ Department of Physics, University of Napoli "Federico II", via Cinthia 9, 80126 Napoli, Italy

⁷ INAF - Osservatorio Astronomico di Capodimonte, via Moiariello 16, 80131 Napoli, Italy

⁸ Millennium Institute of Astrophysics (MAS), Nuncio Monseñor Sótero Sanz 100, Providencia, Santiago, Chile

⁹ SUPA School of Physics and Astronomy, North Haugh, St. Andrews, KY16 9SS, Scotland, UK

¹⁰ Centro Interdisciplinario de Data Science, Facultad de Ingeniería y Ciencias, Universidad Diego Portales, Av. Ejército Libertador 441,

Santiaga, Chile

¹¹ Millennium Nucleus on Transversal Research and Technology to Explore Supermassive Black Holes (TITANS), Gran Bretaña 1111, Playa Ancha, Valparaíso, Chile

12 Department of Astronomy, Faculty of Mathematics, University of Belgrade, Studentski trg 16, 11000 Belgrade, Serbia
 13 Hamburger Sternwarte, Universitat Hamburg, Gojenbergsweg 112, D-21029 Hamburg, Germany
 14 International Gemini Observatory/NSF NOIRLab, Casilla 603, La Serena, Chile
 15 Department of Astronomy, University of Geneva, ch. d' Ecogia 16, 1290, Versoix, Switzerland
 16 Department of Physics, Drexel University, 32 S. 32nd Street, Philadelphia, PA 19104, USA
 17 Departamento de Física, CCNE, Universidade Federal de Santa Maria, 97105-900 Santa Maria, RS,Brazil
 18 Laboratório Interinstitucional de e-Astronomia - LIneA, Rua Gal. José Cristino 77, Rio de Janeiro, RJ - 20921-400, Brazil
 19 Department of Astronomy & Astrophysics, The Pennsylvania State University, University Park, PA 16802, USA
 20 The Institute for Gravitation for and the Cosmos, The Pennsylvania State University, University Park, PA 16802, USA
 21 European Southern Observatory, Karl-Schwarzschild-Strasse 2, 85748 Garching bei München, Germany
 22 Instituto de Astrofísica, Facultad de Ciencias Exactas, Universidad Andrés Bello, Fernández Concha 700, 7591538 Las Condes, Santiago, Chile

²³ Physics Department, Tor Vergata University of Rome, Via della Ricerca Scientifica 1, 00133 Rome, Italy
 ²⁴ INAF Astronomical Observatory of Rome, Via Frascati 33, 00040 Monte Porzio Catone, Italy
 ²⁵ INFN Rome Tor Vergata, Via della Ricerca Scientifica 1, 00133 Rome, Italy
 ²⁶ Centre for Extragalactic Astronomy, Department of Physics, Durham University, South Road, Durham DH1 3LE, UK
 ²⁷ National Radio Astronomy Observatory, 520 Edgemont Road, Charlottsville, VA 22904, USA
 ²⁸ Department of Astronomy, University of Virginia, 530 McCormick Rd, Charlottesville, VA 22904, USA
 ²⁹ Department of Astronomy, University of Michigan, 1085 S University, Ann Arbor, MI 48109, USA

ABSTRACT

The Vera C. Rubin Observatory's Legacy Survey of Space and Time (LSST) will monitor tens of millions of active galactic nuclei (AGNs) for a period of 10 years with an average cadence of 3 days in six broad photometric bands. This unprecedented dataset will enable robust characterizations of AGN UV/optical variability across a wide range of AGN physical properties. However, existing tools for modeling AGN light curves are not yet capable of fully leveraging the volume, cadence, and

Corresponding author: Weixiang Yu wyu@ubishops.ca

multiband nature of LSST data. We present EzTaoX, a scalable light curve modeling tool designed to take advantage of LSST's multiband observations to simultaneously characterize AGN UV/optical stochastic variability and measure interband time delays. EzTaoX achieves a speed increase of $\sim 10^2-10^4\times$ on CPUs over current tools with similar capabilities, while maintaining equal or better accuracy in recovering simulated variability properties. This performance gain enables continuum time-delay measurements for all AGNs discovered by LSST—both in the Wide Fast Deep survey and the Deep Drilling Fields—thereby opening new opportunities to probe AGN accretion-flow geometries. In addition, EzTaoX's multiband capability allows robust characterization of AGN stochastic variability down to hourly timescales, facilitating the identification of accreting low-mass AGNs—such as those residing in dwarf galaxies—through their distinctive variability signatures.

1. MOTIVATION

The UV/optical continuum luminosity of active galactic nuclei (AGNs) exhibit correlated stochastic variability on timescales ranging from hours to years (e.g., Vanden Berk et al. 2004; Sesar et al. 2007; Schmidt et al. 2012). This variability is believed to originate in the accretion disk, potentially driven in part by thermal reprocessing of X-ray photons emitted from the central corona (Krolik et al. 1991) and/or accretion rate fluctuations propagating through the disk (Lyubarskii 1997). For a recent review of the observational properties of AGN variability in the UV/optical and X-ray bands, we refer the reader to Paolillo & Papadakis (2025).

A damped random walk (DRW) process is commonly adopted to model AGN UV/optical light curves (Kelly et al. 2009). The power spectral density (PSD) of a DRW exhibits a broken power-law (PL; $1/f^{\alpha}$) form, where the PL exponent α transitions from zero at low frequencies to two at high frequencies. The point at which this change in PL exponent occurs is known as the break frequency, which corresponds to a characteristic timescale denoted by $\tau_{\rm DRW}$. The asymptotic variability amplitude of the process is denoted by σ_{DRW} . Although the DRW process is a phenomenological model and the precise PSD shape of intrinsic AGN UV/optical variability remains under debate (e.g., Mushotzky et al. 2011; Kasliwal et al. 2015; Smith et al. 2018; Arévalo et al. 2024; Beard et al. 2025; Petrecca et al. 2024; Yu et al. 2025), it continues to be a valuable and widely used tool for modeling AGN light curves because of its adequacy and computational efficiency.

Modeling AGN UV/optical light curves as a DRW has revealed compelling correlations between variability and AGN fundamental properties. Numerous previous investigations have shown that the best-fit $\sigma_{\rm DRW}$ correlates negatively with the Eddington ratio $(L/L_{\rm Edd})$ and bolometric luminosity $(L_{\rm bol})$ of AGNs (e.g., MacLeod et al. 2010; Sánchez-Sáez et al. 2018; Suberlak et al. 2021). Additionally, the characteristic timescale of the DRW model $(\tau_{\rm DRW})$ correlates positively with $M_{\rm BH}$ (e.g., Burke et al. 2021; Wang et al. 2023). These empiri-

cal relations not only provide valuable insights into the physical mechanisms driving AGN variability, but also form the basis for new techniques to estimate AGN fundamental properties using photometric data alone. For example, Burke et al. (2022) leveraged the $\tau_{\rm DRW}-M_{\rm BH}$ correlation to search for low-mass AGNs powered by accreting massive black holes (MBH; $10^5\,M_{\odot} < M_{\rm BH} < 10^7\,M_{\odot}$) at the centers of dwarf galaxies (i.e., $M_{\star} \lesssim 10^{10}\,M_{\odot}$; Greene et al. 2020).

AGN UV/optical variability at longer wavelengths is also often observed to lag behind the variability at shorter wavelengths (Collier et al. 1999; Sergeev et al. 2005). Under the thermal reprocessing scenario, longer-wavelength photons originate from disk annuli located farther from the central supermassive black hole (SMBH) than those emitting shorter-wavelength photons (Shakura & Sunvaev 1973). Consequently, the reprocessed emission at longer wavelengths exhibits longer light-crossing time delays relative to the central irradiating source (Cackett et al. 2007). This specific geometry—in which a compact source near the SMBH (e.g., an X-ray corona) irradiates the accretion disk—is commonly referred to as the lamp-post model. In this framework, the size of the accretion disk can be inferred by measuring the time lags between UV/optical light curves at different wavelengths—a technique known as continuum reverberation mapping (CRM), which probes the geometry of unresolved sources through time-delay measurements (see Cackett et al. 2021, and references therein).

Numerous CRM experiments have reported that AGN accretion disk sizes are systematically larger than those predicted by the standard thin-disk model (e.g., Fausnaugh et al. 2016; Jiang et al. 2017; Jha et al. 2022). Larger-than-expected accretion disk sizes have also been independently inferred from microlensing observations of gravitationally lensed quasars, where the disk half-light radius (i.e., the characteristic size) is inferred from the differential microlensing variability exhibited by the multiple lensed images (e.g., Pooley et al. 2007; Dai et al. 2010; Morgan et al. 2010; Jiménez-Vicente et al. 2014;

Cornachione et al. 2020). It has been suggested that the measured lags may be contaminated by reprocessed UV/optical photons originating in the broad emission-line region (BLR), which lies farther out in the accretion flow (e.g., Korista & Goad 2001; McHardy et al. 2018; Cackett et al. 2018; Lawther et al. 2018). This contamination could cause the observed interband continuum lags to appear longer than those expected from pure disk reprocessing.

In contrast, some studies have argued that accretion disk sizes inferred from CRM are consistent with the standard thin-disk model when factors such as temperature fluctuations within the disk or potential selection biases are properly accounted for (e.g., Dexter & Agol 2011; Mudd et al. 2018; Homayouni et al. 2019; Yu et al. 2020b). Moreover, Kammoun et al. (2021) showed that the standard thin-disk model can reproduce the observed CRM lags when relativistic (special and general) and disk ionization effects are fully included. The accretion disk size discrepancy poses one of the significant challenges to the standard thin-disk model and to our understanding of AGN accretion physics more broadly. A large sample of AGNs with robustly measured CRM lags is required to investigate this issue further. date, however, CRM lags have been successfully measured for only a few hundred AGNs (e.g., Collier et al. 1998; Peterson et al. 1998; Sergeev et al. 2005; Jiang et al. 2017; Homayouni et al. 2019; Mudd et al. 2018; Yu et al. 2020b; Guo et al. 2022).

The Vera C. Rubin Observatory's Legacy Survey of Space and Time (LSST) will significantly advance AGN research by providing high-quality multiband light curves for millions of AGNs spanning a wide range of physical properties and redshifts (Ivezić et al. 2019). LSST's Wide Fast Deep (WFD) survey will monitor $18,000 \, \mathrm{deg^2}$ of sky with an average cadence of three days in six photometric bands (ugrizy), accumulating ~ 800 visits over its 10-year operation. In addition, LSST will observe five Deep Drilling Fields (DDFs), each covering $\sim 10 \, \rm deg^2$ and receiving at least 10 times more visits than the WFD survey. Thousands of AGNs in each DDF will be monitored at sub-day cadence (combining all bands) throughout the decade-long operation (Brandt et al. 2018; Kovačević et al. 2022). The single-visit 5σ limiting magnitudes of LSST reach 23.9, 25.0, 24.7, 24.0, 23.3, and 22.1 in the u, g, r, i, z, and y bands, respectively (Ivezić et al. 2019).

The high-quality light curves provided by LSST will enable robust characterization of AGN UV/optical variability and interband continuum lags. Interband lags can be measured for about one million LSST AGNs (Yu et al. 2020a, Li et al. 2025 submitted), allowing de-

tailed investigations of the accretion disk size problem as a function of AGN properties such as $L_{\rm Edd}$ and $M_{\rm BH}$, and offering new insights into the physical origin of continuum lags. Meanwhile, stochastic variability parameters—such as characteristic timescales and amplitudes—extracted from LSST light curves will enable reliable AGN classification (e.g., Kozłowski et al. 2010; Butler & Bloom 2011; MacLeod et al. 2011; Peters et al. 2015; De Cicco et al. 2021; Sánchez-Sáez et al. 2021; Savić et al. 2023; Sánchez-Sáez et al. 2023). For example, variability-based methods are more effective than SED-based methods at identifying low-luminosity and low-mass AGNs (e.g., in dwarf galaxies), where host-galaxy starlight contamination is significant (e.g., Baldassare et al. 2017; Ward et al. 2022; Bernal et al. 2025). A complete census of low-luminosity is essential for understanding AGN evolution across cosmic time (Richards et al. 2006), while a comprehensive inventory of low-mass AGNs is critical for constraining the formation pathways of SMBHs (see Greene et al. 2020, and references therein).

However, existing AGN light curve analysis tools are not well-prepared to fully exploit the scale and richness of LSST observations. Current tools/methods used to characterize AGN UV/optical variability typically operate on single-band light curves and lack the ability to incorporate multiband information (e.g., Vaughan et al. 2003; Kelly et al. 2009, 2014; Kozłowski 2016; Yu & Richards 2022). This limitation prevents the effective utilization of LSST's multiband coverage for improved characterization of AGN variability. Tools/methods commonly used to measure interband lags generally fall into two categories. The first includes techniques that estimate lags by computing the cross-correlation function (CCF) between light curves; the CCF reaches its maximum when one light curve is shifted relative to the other by an amount corresponding to the intrinsic lag (e.g., Gaskell & Peterson 1987; Edelson & Krolik 1988; Alexander 1997). These methods are typically computationally efficient, but are limited to lag estimation and do not provide a full characterization of the underlying variability process. The second consists of methods that model each observed light curve as the convolution of an unknown driving continuum with a time-lag distribution, represented by a transfer function (e.g., Zu et al. 2011; Li et al. 2016; Starkey et al.

¹ When applied to a single-band light curve and its shifted copies, the CCF method yields its autocorrelation function (ACF), which can be used to characterize AGN variability (e.g., Raiteri et al. 2021a,b).

2016; Donnan et al. 2021). This is expressed as,

$$y(t) = \int d\tau \, \Psi(\tau) \, y_{\text{drive}}(t - \tau), \tag{1}$$

where $y_{\rm drive}(t-\tau)$ denotes the flux of the underlying driving continuum at $t-\tau$, and $\Psi(\tau)$ represents the corresponding transfer function. JAVELIN is a representative tool in this category (Zu et al. 2013). It models the driving continuum as a DRW process and adopts a top-hat profile for the transfer function. While such methods provide a more comprehensive treatment by jointly modeling variability and interband lags, they are often computationally demanding.

Many recent investigations have turned to machine learning (ML) techniques to develop more scalable methods for analyzing AGN light curves (e.g., Fagin et al. 2024; Li et al. 2024). In these approaches, deep neural networks are trained on simulated light curves and are tasked with recovering the underlying variability characteristics and/or the physical parameters used to generate the simulations. However, the reliability of such methods hinges on the assumption that the models used to generate the training data accurately represent both the variability physics and the observational conditions (e.g., cadence, photometric uncertainty)—an assumption rarely satisfied in practice. For example, Li et al. (2024) show that the AGN physical parameters (e.g., $M_{\rm BH}$) predicted by their simulation-based inference model (Cranmer et al. 2020) can be biased by up to 0.5 dex when the test light curves are five times noisier than those used for training.

In this paper, we present EzTaoX—a scalable and flexible AGN light curve modeling tool that leverages LSST's multiband observations to simultaneously infer the properties of the underlying stochastic variability and the lags between photometric bands (Yu & Burke 2025). The name of EzTaoX combines three elements: "Ez", a homophone of easy; "Tao" referencing the Chinese philosophical and religious tradition of Taoism, commonly translated as "the Way"; and "X" denoting that the code is implemented in JAX a high-performance numerical computing library developed by Google. EzTaoX achieves a speed increase of $\sim 10^2 - 10^4 \times$ on CPUs compared to existing tools with similar capabilities (e.g., JAVELIN), making it feasible to perform both stochastic variability characterization and interband continuum lag measurements for all AGNs discovered by LSST. Furthermore, EzTaoX's multiband capability enables robust constraints on stochastic variability timescales (e.g., τ_{DRW}) down to one hour with the LSST WFD cadence, facilitating the identification of low-mass AGNs—such as those residing in dwarf galaxies—which are expected to exhibit characteristic $\tau_{\rm DRW}$ ranging from hours to days (Burke et al. 2021; Wang et al. 2023).

The rest of the paper is organized as follows. Section 2 describes the methods and algorithms implemented in EzTaoX for characterizing AGN stochastic variability and interband continuum lags. Section 3 presents the performance of EzTaoX in terms of computational scalability and its robustness in recovering stochastic variability parameters and interband lags. In Section 4, we discuss the scientific opportunities enabled by EzTaoX, limitations of the current implementation, and potential directions for future development. Finally, we summarize our findings and conclude in Section 5.

2. LIGHT CURVE MODELING METHOD & IMPLEMENTATION

EzTaoX models AGN UV/optical stochastic variability as a Gaussian processes (GP), a method commonly adopted in AGN variability analysis (e.g., Press et al. 1992; Kelly et al. 2009; Kozłowski et al. 2010; Wilkins 2019; Griffiths et al. 2021; Yu et al. 2022; Stone et al. 2022; Zhang et al. 2023; McLaughlin et al. 2024). Since the flux light curves of accreting compact objects typically follow a lognormal distribution (e.g., Uttley & McHardy 2001; Gaskell 2004; Giebels & Degrange 2009; MacLeod et al. 2012; De Cicco et al. 2022), we emphasize that GP modeling is best applied to magnitude light curves, which follow a Gaussian distribution.²

Given a single band AGN light curve, a GP treats the intrinsic brightness of the AGN at each point in time as a Gaussian random variable and captures the temporal correlations between observations through a kernel function $k(t_i, t_j)$, which defines the covariance between the Gaussian variables at any two timestamps t_i and t_j (Rasmussen & Williams 2006; Aigrain & Foreman-Mackey 2023).

The likelihood function of a GP given a set of observations \mathbf{y} is,

$$\ln \mathcal{L} = -\frac{1}{2} (\mathbf{y} - \boldsymbol{\mu})^{\top} \mathbf{K}^{-1} (\mathbf{y} - \boldsymbol{\mu})$$

$$-\frac{1}{2} \ln \det(\mathbf{K}) - \frac{N}{2} \ln(2\pi)$$
(2)

where μ is the mean vector with its entries equal to the mean of \mathbf{y} , and N is the total number of observations in \mathbf{y} . \mathbf{K} is the GP covariance matrix, with each entry given by

$$K_{ij} = k(|t_j - t_i|) + \sigma_i^2 \,\delta_{ij},\tag{3}$$

² Gúrpide & Middleton (2025) demonstrated that even when the light curves follow a lognormal distribution, the simulated GP parameters can be recovered without significant bias.

where k is the aforementioned kernel function, and t_i and t_j are the timestamps of the $i^{\rm th}$ and the $j^{\rm th}$ observation, respectively. The parameter σ_i denotes the measurement uncertainty of the $i^{\rm th}$ observation, and δ_{ij} is the Kronecker delta. The widely-adopted DRW model can expressed as a GP with the following kernel function:

$$k_{\text{DRW}}(|\Delta t|) = \sigma_{\text{DRW}}^2 e^{-|\Delta t|/\tau_{\text{DRW}}},$$
 (4)

where Δt gives the time difference between any two observations in a light curve.

EzTaoX performs multiband modeling and interband lag measurements by treating mean-subtracted light curves from different photometric bands as scaled and time-shifted realizations of a shared underlying GP. This approach is mathematically equivalent to adopting a Dirac delta function as the transfer function in Equation 1, with the delta function centered at a constant temporal offset. Under this framework, light curves from different photometric bands and different photometric surveys can be combined and modeled using a one-dimensional GP. This approach can in principle accommodate any number of photometric bands, although the number of free parameters grows with the number of distinct bands.

The corresponding kernel function for any two observations in such a merged light curve is,

$$k(|t_j - t_i|) = S_1 S_2 k_{\text{latent}}(|t_j - t_i - \tau_{\text{lag}}|), \qquad (5)$$

where k_{latent} denotes the kernel of the underlying latent GP. S_1 and S_2 are the variability-amplitude scaling factors for the corresponding photometric bands, and τ_{lag} represents the relative time lag between them. The variability amplitude in each band is obtained by multiplying the latent GP amplitude by the corresponding scaling factor. This class of kernel functions, as expressed in Equation 5, has seen broad application in astronomical time series analysis (e.g., Gordon et al. 2020; Villar et al. 2021). To evaluate the likelihood of the multiband model for a given light curve, we shift the light curve in different bands by their trial τ_{lag} relative to the reference band, and compute Equation 2 using a kernel that assumes no intrinsic lag between bands (i.e., setting $\tau_{\text{lag}} = 0$ in Equation 5). In this way, the GP parameters and the interband lags are fitted jointly.

EzTaoX is built on top of tinygp³—a GP modeling framework developed using JAX.⁴ JAX is a high-performance numerical computing library that combines

automatic differentiation, just-in-time (JIT) compilation, and hardware acceleration to empower scalable machine learning and scientific computing. tinygp leverages these features of JAX and re-implements the novel celerite algorithm introduced by Foreman-Mackey et al. (2017) in JAX. When a kernel function can be expressed as a mixture of exponentials, the celerite algorithm can evaluate the GP likelihood function with $\mathcal{O}(N)$ computational scaling, a significant efficiency enhancement over the standard $\mathcal{O}(N^3)$ scaling associated with direct likelihood evaluation (Foreman-Mackey et al. 2017). EzTaoX takes advantage of the JAX-based implementation of the celerite algorithm to provide a scalable solution for multiband light curve modeling of AGNs.

PSD shapes exhibited by the light curves of accreting black holes can be effectively modeled with celerite GP kernels. For example, the continuous-time autoregressive moving-average (CARMA) process—commonly used as a more flexible alternative to the DRW process has an equivalent celerite implementation (Roux 2002; Kelly et al. 2014; Kasliwal et al. 2017; Moreno et al. 2019; Yu et al. 2022). A CARMA(p, q) process combines an autoregressive process of order p with a moving-average process of order q, and its PSD can be expressed as a weighted sum of modified Lorentzians. The DRW process is a special case of a CARMA process with p = 1 and q = 0. For a detailed description of CARMA modeling, we refer the reader to Kelly et al. (2014). More recently, Lefkir et al. (2025) introduced an algorithm for approximating arbitrary broken PL PSDs using a sum of multiple celerite kernels, thereby enhancing the interpretability and flexibility of GP-based modeling for AGN light curves. Moreover, celerite-based kernels can be freely combined through addition and multiplication to model more complex covariance structures, while retaining the $\mathcal{O}(N)$ computational scaling. All such kernels can be used for simultaneous multiband variability characterization and interband lag measurements.

3. EzTaoX PERFORMANCE

In this section, we evaluate the robustness and scalability of EzTaoX and compare it to the widely adopted tool JAVELIN. Since JAVELIN supports only the DRW kernel for modeling the driving continuum variability during lag measurement, all performance experiments conducted in this work assume a DRW model for the underlying AGN continuum stochastic variability. Section 3.1 demonstrates EzTaoX's robustness in recovering input interband lags and DRW parameters from simulated LSST WFD light curves. In Section 3.2 and

³ https://github.com/dfm/tinygp

⁴ https://github.com/jax-ml/jax

Light Curve Set	g -band $ au_{ m DRW}$	g -band σ_{DRW}	Interband Lag	Band	Duration
	[day]	[mag]	[day]		[year]
One	100	0.112	Uniform(0.01, 10)	g, r	3, 10
Two	LogUniform(0.01, 500)	0.112	$0.01 \times \tau_{\mathrm{DRW}}$	u, g, r	3
Three	100	LogUniform(0.02, 0.2)	1	u,g,r	3

Table 1. Input Parameters for Simulated LSST WFD AGN Light Curves

Section 3.3, we apply EzTaoX to continuum reverberation mapping light curves of real AGNs and compare the resulting lag measurement with values reported in the literature. Finally, Section 3.4 presents computational benchmarking results for EzTaoX.

3.1. Robustness: A Test Using Simulated LSST WFD Light Curves

In this section, we simulate realistic LSST WFD light curves, and assess how well EzTaoX recovers both the simulated interband lags and stochastic variability parameters. Section 3.1.1 describes the light curve simulation process and the sets of input parameters (see Table 1). In Section 3.1.2, we show that EzTaoX is capable of retrieving interband lags with accuracy comparable to that of JAVELIN. Section 3.1.3 and Section 3.1.4 demonstrates the robustness of EzTaoX in recovering input stochastic variability parameters (i.e. $\tau_{\rm DRW}$ and $\sigma_{\rm DRW}$). We emphasize that the goal of the experiments in this section is to demonstrate the overall capability of EzTaoX, rather than to perform a full parameter-space study or to investigate its systematics. Nonetheless, the code for generating and fitting simulated LSST light curves will be made available upon request, allowing interested reader to further explore the robustness of EzTaoX under different combinations of input parameters.

3.1.1. Light Curve Simulation

We adopt the DRW model to simulate AGN light curves in individual LSST bands. We start by simulating DRW light curves in each LSST band with a 30-second cadence; this 30-second cadence is chosen to match the 30-second exposure time of each LSST single visit (Ivezić et al. 2019). The input DRW parameters across different bands are correlated according to the wavelength-dependent power-law relations presented in MacLeod et al. (2010). More specifically,

$$\tau_{\rm DRW} \propto \lambda^{0.17}, \quad \sigma_{\rm DRW} \propto \lambda^{-0.479},$$
(6)

where λ is the effective wavelength of the LSST filters (Ivezić et al. 2019). We then simulate continuum

lags by offsetting light curves in redder band in time with respect to light curves in bluer bands. Finally, we downsample the simulated 30-second cadence light curve to the observing cadence of the WFD survey.

The observational noise is simulated by adding random values drawn from Gaussian distributions with mean zero and variance $\sigma_{\rm LSST}^2$. The parameter $\sigma_{\rm LSST}$ is the expected photometric error of LSST, and it can be approximated using

$$\sigma_{\rm LSST}^2 = \sigma_{\rm sys}^2 + \sigma_{\rm rand}^2,\tag{7}$$

where $\sigma_{\rm sys}$ is the systematic photometric error and $\sigma_{\rm rand}$ is the random photometric error. LSST aims to achieve a $\sigma_{\rm sys} < 0.005$ mag (Ivezić et al. 2019); we set $\sigma_{\rm sys}$ to 0.005 mag in our simulation. The random photometric error ($\sigma_{\rm rand}$) is expected to scale as

$$\sigma_{\text{rand}}^2 = (0.04 - \gamma)x + \gamma x^2 \,(\text{mag}^2), \quad x = 10^{0.4(m - m_5)},$$
(8)

where m_5 is the 5σ limiting magnitude in a given band (for point sources), and γ is a band-dependent factor (Ivezić et al. 2019). Following Ivezić et al. (2019), we set γ to 0.038 for u-band and to 0.039 for other LSST bands.

The observing cadence and the expected m_5 at any location on the sky are predicted by LSST operation simulations (OpSims) using MAF (Marshall et al. 2017). In this work, we adopt the operation simulation version baseline_v4.0_10yrs. All our simulated AGNs also assume a fiducial g-band mean magnitude of 21 ($\sim 1\%$ photometric accuracy) and mean u-g and g-r colors of 0.1 mag (Richards et al. 2001; Temple et al. 2021). An example light curve from the first set is shown in Figure 1.

We generate three sets of multiband LSST light curves using different input distributions for the interband lags and DRW parameters. The distributions of input parameters are also summarized in Table 1. Each set consists of 975 simulated light curves with their cadence and m_5 retrieved from 975 unique locations uniformly sampled in the WFD footprint. To construct this sample, we first generate a uniform grid with 5° spacing in both

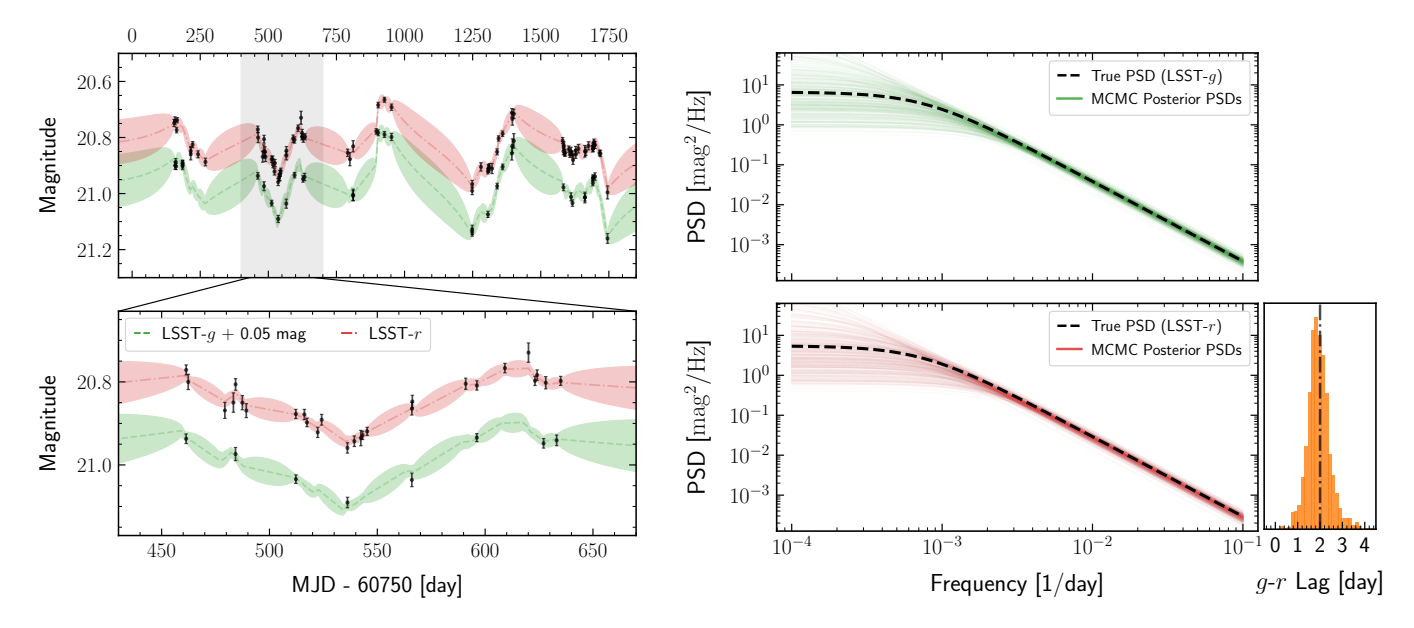


Figure 1. Left: Example LSST WFD light curves simulated using the DRW model. The g- and r-band light curves have fiducial mean magnitudes of 21 and 20.9, respectively. Right: The true (dashed curves) and recovered (colored solid curves) PSDs. The recovered PSDs are generated using random draws of the MCMC posterior distribution. The orange histogram in the bottom right panel shows the posterior distribution of the recovered g-r lag, with the dash-dotted vertical line indicating the true simulated lag of 2 days.

RA and Dec, spanning $0^{\circ} < \text{RA} < 360^{\circ}$ and $-75^{\circ} < \text{Dec} < +15^{\circ}$. We then select grid points that receive between 600 and 1000 visits in all six photometric bands. The final simulated full 10-year light curves have median numbers of 53, 65, and 171 epochs in the u, g, and r bands, respectively. When only the first three years of data are considered, these numbers drop to 13, 19, and 50 epochs.

The first set aims to evaluate EzTaoX's ability to recover interband lags (see Section 3.1.2), and the light curves consist of simulated LSST observations in g and r bands. The g-r lag for each multiband light curve is uniformly sampled between 0.01 day and 10 days, while the input g-band $\tau_{\rm DRW}$ and $\sigma_{\rm DRW}$ are fixed at fiducial values of 100 days and 0.112 mag, respectively. These choices of $\tau_{\rm DRW}$ and $\sigma_{\rm DRW}$ are representative of those measured from typical quasar (i.e., high luminosity AGN) UV/optical light curves (e.g., Vanden Berk et al. 2004; MacLeod et al. 2010).

The second set tests EzTaoX's ability to recover the DRW characteristic timescale $\tau_{\rm DRW}$ (see Section 3.1.3), and the light curves consist of simulated LSST observations in u, g, and r bands. The input g-band $\tau_{\rm DRW}$ is randomly sampled from a log-uniform distribution between 0.01 day and 500 days, while the g-band $\sigma_{\rm DRW}$ is set to a fiducial value of 0.112 mag. The u-g and g-r lags are set to 1% of the g-band $\tau_{\rm DRW}$.

The third set evaluates EzTaoX's ability to recover the DRW asymptotic variability amplitude σ_{DRW} (see Sec-

Table 2. MCMC Prior for EzTaoX Parameters

Parameter	Prior Distribution		
$\tau_{ m DRW}$ [day]	$LogUniform(10^{-4}, 10^4)$		
$\sigma_{ m DRW} \ [{ m mag}]$	LogUniform(0.01, 2)		
$S_{ m band}$	LogUniform(0.1, 10)		
$\tau_{\mathrm{lag}} \; [\mathrm{day}]$	Uniform(-15, 25)		
$\mu_{\rm band} \ [{ m mag}]$	Normal(0, 0.1)		

NOTE—The normal distribution follow the notation Normal(μ , σ), where μ is the mean, and σ is the width.

tion 3.1.4), and the light curves consist of simulated LSST observations in u, g, and r bands. The input g-band σ_{DRW} is randomly sampled from a log-uniform distribution between 0.02 mag and 0.2 mag, while the g-band τ_{DRW} is set to a fiducial value of 100 days. The u-g and g-r lags are set to 1 day.

3.1.2. Recovery of Interband Lag

We run EzTaoX on the first set of simulated light curves to extract the lag between the g- and r-band ($\tau_{\rm gr}$), after subtracting the mean from each single-band light curve. The EzTaoX light curve model includes seven parameters: $\tau_{\rm DRW}$, $\sigma_{\rm DRW}$, $S_{\rm g}$, $S_{\rm r}$, $\mu_{\rm g}$, $\mu_{\rm r}$, and $\tau_{\rm gr}$. Here, $S_{\rm g}$ and $S_{\rm r}$ are the GP kernel scaling factors for g- and r-

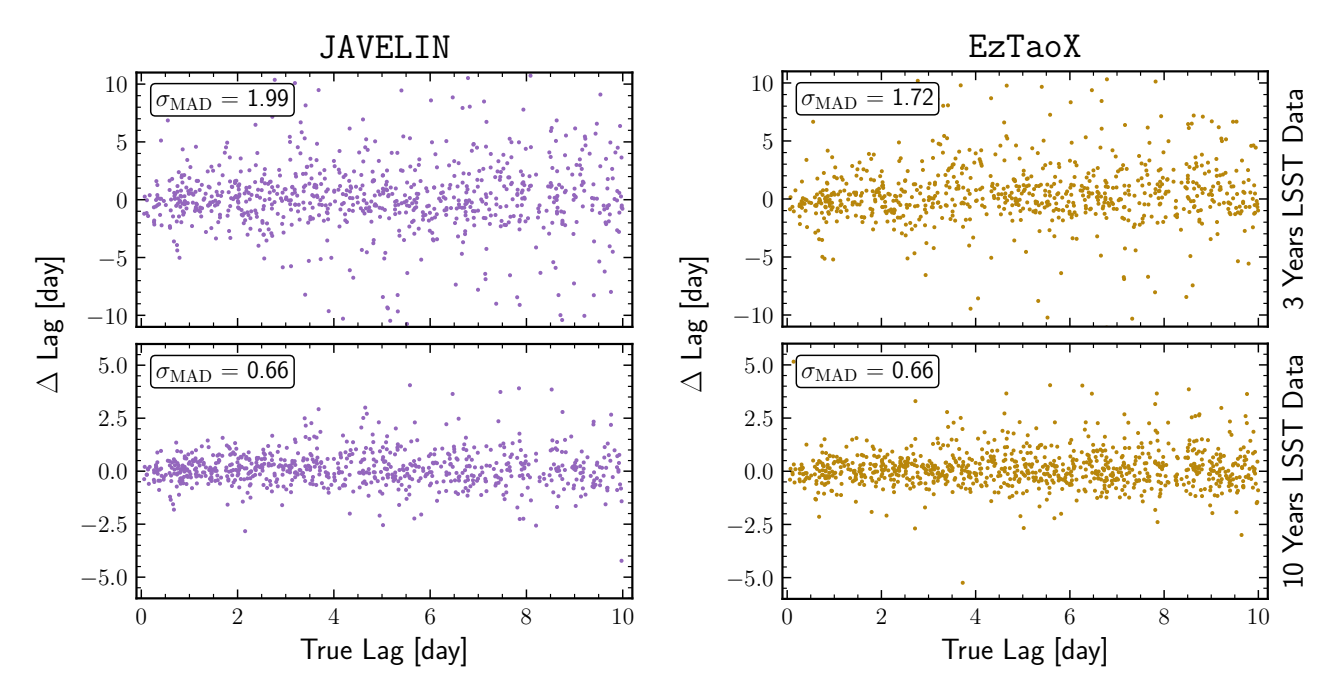


Figure 2. Comparison of g-r lags recovered using JAVELIN (left) and EzTaoX (right) from simulated LSST WFD light curves. Both JAVELIN and EzTaoX yield comparable results in terms of lag measurement accuracy. *Top*: The difference between the recovered and true lags (Δ lag) as a function of the true lag, based on fits obtained using only the first 3 years of WFD observations. The dispersion of Δ lag, computed using the median absolute deviation (MAD), is indicated in the top-left corner of each panel. *Bottom:* Same as the top panels, but using the full 10 years of WFD observations for inference.

band observations (see Equation 5), while $\mu_{\rm g}$ and $\mu_{\rm r}$ are the mean magnitudes of the g- and r-band light curves, respectively. As part of the EzTaoX fitting process, we first compute the maximum likelihood estimates (MLEs) of the model parameters, and use the them to initialize the Markov Chain Monte Carlo (MCMC) sampler for posterior sampling. The adopted MCMC priors are listed in Table 2 and are fixed throughout the analysis unless stated otherwise. The prior ranges are chosen according to the light curve properties. For example, the lower limit for $\tau_{\rm DRW}$ is set to ~ 10 times smaller than the minimum time separation between any two observations, while the upper limit is ~ 10 times larger than the light curve length. MCMC sampling is performed using the gradient-based No-U-Turn Sampler (NUTS: Hoffman & Gelman 2011), with a single chain run for 10^4 steps following 10^3 warm-up steps. The posterior median of τ_{DRW} is taken as the point estimate.

We also apply JAVELIN to the first set of simulated light curves to measure $\tau_{\rm gr}$. The JAVELIN light curve model includes five parameters: $\tau_{\rm DRW}$, $\sigma_{\rm DRW}$, $s_{\rm gr}$, $w_{\rm gr}$, and $\tau_{\rm gr}$. Here, $s_{\rm gr}$ and $w_{\rm gr}$ describe the scale and width, respectively, of the top-hat transfer function for the g- r lag. JAVELIN employs a two-step fitting procedure: it first generates a distribution of $\tau_{\rm DRW}$ and $\sigma_{\rm DRW}$ by fitting the light curve of a chosen band via MCMC sampling, and then uses that distribution as a prior for the

DRW parameters while simultaneously fitting both the DRW parameters and the interband lags from the light curves in all bands. In the first step, the light curve in the bluest band is typically used, as JAVELIN assumes that redder-band light curves are convolved versions of it; here we use the g-band light curve. For MCMC sampling, JAVELIN employs the affine-invariant ensemble sampler (Goodman & Weare 2010) as implemented in emcee (Foreman-Mackey et al. 2013). In the first step we follow the default configuration, while in the second step we run the sampler with 100 walkers, 500 burn-in steps, and 3000 sampling steps. We also set the prior bound for $\tau_{\rm DRW}$ to $[10^{-4}, 10^4]$ days and for $\tau_{\rm gr}$ to [-15, 25] days. The posterior median of $\tau_{\rm gr}$ is reported as the final point estimate.

We clean the sample of best-fit EzTaoX and JAVELIN lags by removing those associated with non-convergent MCMC chains. Specifically, we discard fits in which the MCMC chain for $\tau_{\rm gr}$ yields fewer than 400 effective samples $(n_{\rm eff})$, following the recommendation of Vehtari et al. (2021) for selecting converged chains. Approximately 20% of the 3-year and 7% of the 10-year EzTaoX fits are removed by this criterion, while ~20% of the JAVELIN fits are removed from both the 3-year and 10-year data. Examined as a function of the input $\tau_{\rm gr}$, the fraction of discarded JAVELIN fits increases with increasing true $\tau_{\rm gr}$; in contrast, the fraction of discarded

EzTaoX fits remains relatively constant across the range of input $\tau_{\rm gr}$. We discuss this effect in more detail in Section 4.3.

Based on the cleaned samples, EzTaoX and JAVELIN yield comparable results for lag measurement accuracy. Figure 2 presents the difference between the recovered lag and the true simulated lag (Δ lag) as a function of the true lag. The left column shows results from JAVELIN, while the right column displays results from EzTaoX. The top row corresponds to fits obtained using only the first 3 years of simulated LSST light curves, and the bottom row shows results based on the full 10-year simulated dataset. The dispersion in Δ lag is $\lesssim 2$ days when using 3 years of data and improves to $\lesssim 0.7$ day with the full 10-year dataset. These dispersions are consistent with the mean uncertainties derived from the MCMC posterior distributions.

3.1.3. Recovery of Stochastic Variability Timescale

We follow the same strategy described in the previous section to fit the second set of simulated light curves. We apply EzTaoX to multiband light curves containing observations in u, g, and r bands, as well as to light curves with observations in only one of the three bands. We use the same set of MCMC configurations as those employed in Section 3.1.2. When fitting the multiband light curves, we observed that MCMC chains take significantly longer to converge when the true interband lag is shorter than a few hours. This behavior may be driven by the minimum interband cadence (i.e., u-g, g-r, etc.) of ~ 40 minutes, which hampers reliable lag measurements on hourly timescales and below. To mitigate this issue, and without loss of generality, we fix the interband lags to zero when the MLE of $\tau_{\rm DRW}$ fall below 10 days corresponding to a simulated lag of ~ 2.5 hours. We exclude fits that either exhibit poorly-converged MCMC chains ($n_{\rm eff} < 400$) or yield a best-fit $\tau_{\rm DRW}$ more than an order of magnitude smaller than the minimum cadence. About 5% of EzTaoX fits are removed by these two criteria.

Combining observations from multiple bands leads to noticeable improvements in constraints on the DRW characteristic timescale ($\tau_{\rm DRW}$), owing to the enhanced temporal coverage of multiband light curves. The left panel of Figure 3 displays the recovered $\tau_{\rm DRW}$ as a function of the input value. The blue, green, and red shaded regions mark the central 68% intervals of $\tau_{\rm DRW}$ recovered using u-, g-, or r-band observations, respectively, while the yellow hatched region indicates the interval when all three bands are fitted jointly. Including all three bands substantially reduces the scatter in the recovered $\tau_{\rm DRW}$. The right panel of Figure 3 further il-

lustrates this gain, showing the mean 1σ uncertainty—defined as half the 68% posterior interval from MCMC—as a function of input $\tau_{\rm DRW}$. To test the robustness of these uncertainties, we computed the fraction of fits whose 1σ posterior intervals include the true input $\tau_{\rm DRW}$; for well-calibrated uncertainties this should be close to 68%. Across input values, the coverage fraction ranges from 60% to 80% for both single- and multiband fits. As an additional check, we fit another set of light curves simulated with g-band $\sigma_{\rm DRW}=0.06$ mag and show in Appendix A that EzTaoX still yields unbiased estimates of $\tau_{\rm DRW}$.

To better demonstrate the advantages of multiband fitting, we refit the second set of simulated light curves after removing revisits occurring within 1 hr in any given band. This removal mimics a scenario in which intranight observations must be stacked to detect faint variable sources against host-galaxy starlight—such as lowluminosity and low-mass AGNs, which are expected to exhibit shorter characteristic variability timescales than typical quasars (e.g., Burke et al. 2021). Figure 4 displays the recovered $\tau_{\rm DRW}$ as a function of the input value. When using only u- or g-band observations, the recovered τ_{DRW} is systematically biased for input values below a few days. In contrast, combining u- and g-band data allows τ_{DRW} to be recovered without bias down to hourly timescales. Furthermore, MCMC chains fail to converge (i.e., $n_{\rm eff} < 400$) in more than 40% of the single-band fits, whereas this fraction decreases to only 7% for the multiband fits, underscoring the improved reliability of multiband fitting. The multiband capability of EzTaoX thus enables robust selection of low-luminosity and low-mass AGNs based on variability, particularly those with intrinsically faint emission and stochastic variability characterized by τ_{DRW} values of just hours to days.

We also run JAVELIN on the second set of light curves with observations in all three bands. To improve convergence, we increase the number of MCMC sampling steps from 3000 to 10^4 . In the first fitting step, we use the r-band light curve to generate the prior distribution of τ_{DRW} and σ_{DRW} , since the r-band provides the densest temporal sampling and lowest photometric uncertainty. As shown in Appendix B, the final DRW parameter distributions recovered by JAVELIN depend on the photometric band used in the first step, with the rband yielding the most reliable results. As with EzTaoX, we find that the MCMC chains exhibit poor convergence when the true interband lag is shorter than a few hours. To mitigate this issue, and without loss of generality, we fix the interband lags to zero when the MLE of $\tau_{\rm DRW}$ falls below 10 days. Finally, we apply the same sample-

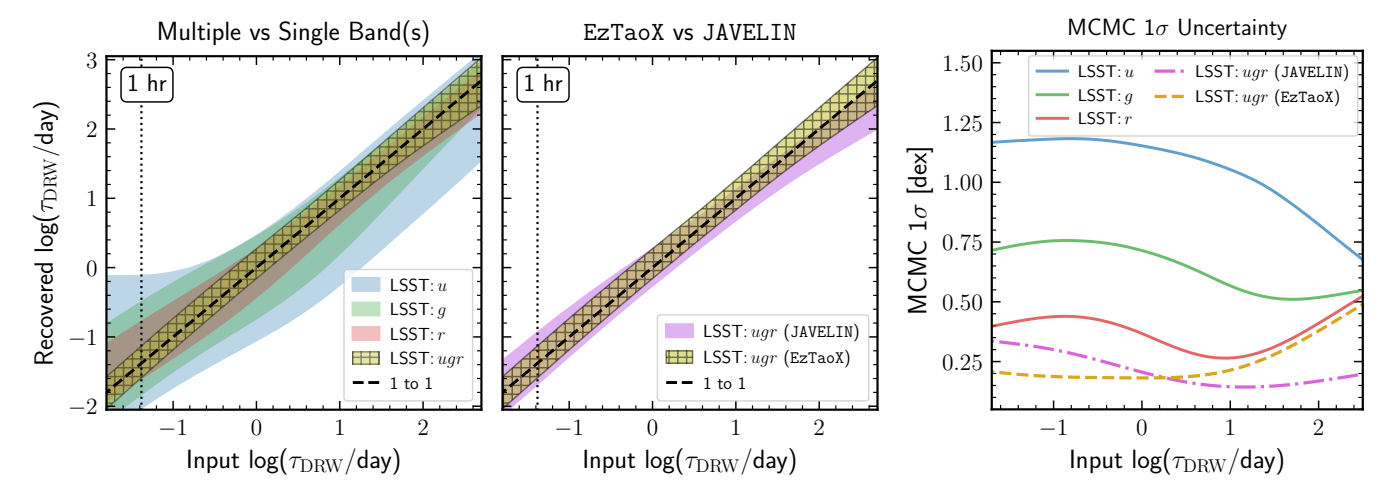


Figure 3. Comparison of recovered and input τ_{DRW} based on 3 years of simulated LSST WFD observations. EzTaoX's multiband fitting capability yields more robust and accurate estimates of τ_{DRW} . Left: Comparison of τ_{DRW} recovered from single-band vs. multiband observations. The blue, green, and red shaded regions represent the central 68% intervals of the recovered τ_{DRW} when using only u-, g-, or r-band observations, respectively. The yellow hatched region indicates the corresponding central 68% interval when observations from all three bands (u, g, and r) are used jointly in the fitting. Using data from all three bands, EzTaoX can robustly recover τ_{DRW} down to 1 hr (marked by the vertical dotted black line), and the associated uncertainty is noticeably reduced in comparison to single-band fits. Middle: Comparison of multiband inference with EzTaoX and JAVELIN. The results show that τ_{DRW} recovered by JAVELIN are systematically biased when the true $\log(\tau_{\text{DRW}}/\text{day})$ exceeds ~ 1.5 ($\tau_{\text{DRW}} \sim 30$ days). The purple region denotes the central 68% intervals of τ_{DRW} recovered by JAVELIN. Right: The mean MCMC 1σ uncertainty (defined as one half of the central 68% credible interval) for τ_{DRW} demonstrates the improved precision in τ_{DRW} recovery achieved through multiband fitting. However, the MCMC 1σ uncertainty from JAVELIN is clearly underestimated at $\log(\tau_{\text{DRW}}/\text{day}) \gtrsim 1.5$, provided with the systematic biases shown in the middle panel.

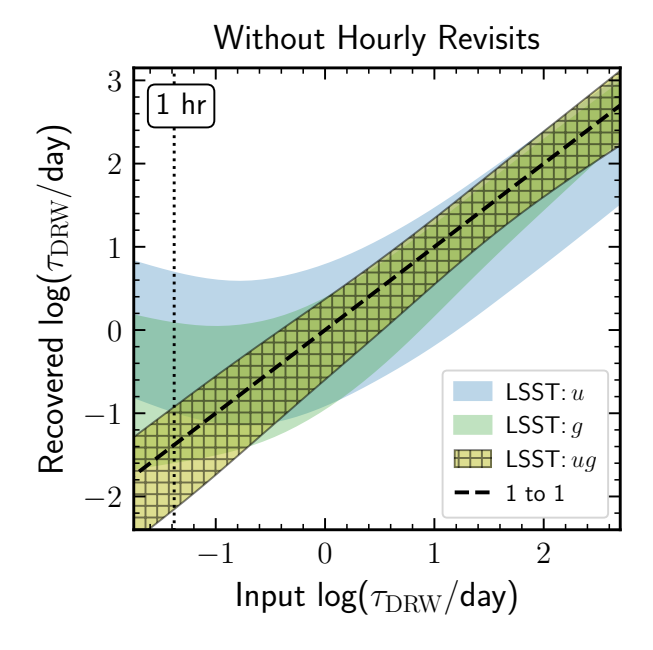


Figure 4. Comparison of recovered and input τ_{DRW} from simulated LSST WFD light curves without hourly revisits. When the input τ_{DRW} is less than a few days, estimates recovered using only the u- or g-band observations show systematic bias. In contrast, combining both u- and g-band observations yields unbiased τ_{DRW} estimates down to hourly timescales.

cleaning cuts used for ${\tt EzTaoX}$, which remove about 5% of the JAVELIN fits.

JAVELIN produces biased estimates of τ_{DRW} from our simulated LSST WFD light curves. The middle panel of Figure 3 compares the recovered and true τ_{DRW} . The purple region denotes the central 68% interval of JAVELIN recoveries, the hatched yellow region shows the corresponding interval for EzTaoX recoveries, and the dashed black line marks the one-to-one relation. For true $\tau_{\mathrm{DRW}} \lesssim 3$ days, JAVELIN slightly overestimates the values, whereas for $\gtrsim 30$ days it underestimates them. Moreover, the MCMC-derived uncertainties from JAVELIN are underestimated for true $\tau_{\rm DRW} \gtrsim 30$ days. The purple dash-dotted curve in the right panel of Figure 3 shows the mean 1σ interval from the posterior, which is clearly too small in this regime, consistent with the fact that fewer than 50% of the fits recover the true input within 1σ .

3.1.4. Recovery of Stochastic Variability Amplitude

We fit the third set of light curves with observations in all three bands using both EzTaoX and JAVELIN, adopting the same priors and MCMC setup as in Section 3.1.3. We exclude fits that either exhibit poorly-converged MCMC chains ($n_{\rm eff} < 400$) or yield a best-fit value of $\sigma_{\rm DRW} < 0.003$ mag, an order of mag-

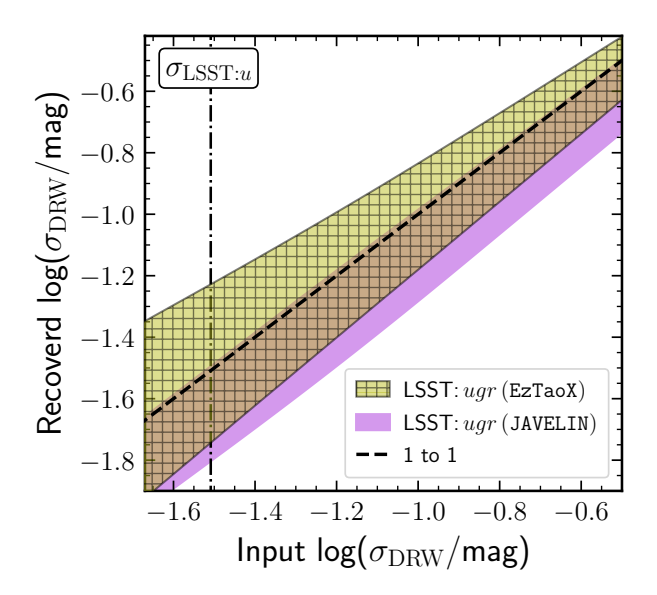


Figure 5. Comparison of recovered and input $\sigma_{\rm DRW}$ from multiband light curves using u-, g-, and r-band observations with EzTaoX and JAVELIN. The hatched yellow region and the purple region represent the central 68% interval of EzTaoX-and JAVELIN-inferred $\sigma_{\rm DRW}$, respectively. EzTaoX yields unbiased estimates of $\sigma_{\rm DRW}$ across the full simulated range, from levels comparable to the photometric uncertainty up to ~ 0.2 mag. In contrast, JAVELIN fails to recover $\sigma_{\rm DRW}$ when it approaches a few times the u-band photometric uncertainty, as marked by the vertical dash-dotted line.

nitude below the simulated photometric uncertainty (e.g., $\sigma_{\mathrm{LSST}:u}\approx 0.03$ mag). This removes $\sim\!5\%$ of the EzTaoX and JAVELIN fits.

EzTaoX is able to recover σ_{DRW} without bias down to levels comparable to the photometric uncertainty of the simulated observations. Figure 5 shows the recovered versus input σ_{DRW} . The hatched yellow region and the purple region denote the central 68% intervals of $\sigma_{\rm DRW}$ recovered by EzTaoX and JAVELIN, respectively. Across the full range of simulated σ_{DRW} , EzTaoX provides unbiased estimates. In contrast, JAVELIN systematically underestimates $\sigma_{\rm DRW}$, with values falling below the one-to-one relation (dashed diagonal). We suspect the bias likely arise from the underestimation of $\tau_{\rm DRW}$ seen in the middle panel of Figure 3. Because $\tau_{\rm DRW}$ and $\sigma_{\rm DRW}$ are correlated, JAVELIN yields biased estimates of both parameters when the true τ_{DRW} exceeds ~30 days in a 3-year light curve. Finally, to demonstrate the robustness of EzTaoX in this regime, we simulate and fit an additional set of light curves with $\tau_{\rm DRW} = 200$ days; the results are presented in Appendix A.

3.2. A Test Using Continuum Reverberation Mapping Light Curves of NGC 5548

The AGN Space Telescope and Optical Reverberation Mapping (STORM) project is an intensive multi-wavelength monitoring campaign targeting NGC 5548, a well-studied Seyfert galaxy (De Rosa et al. 2015; Edelson et al. 2015; Fausnaugh et al. 2016). This campaign combines observations from the *Hubble Space Telescope* (HST), the Neil Gehrels Swift Observatory (Swift hereafter; Gehrels et al. 2004), and a network of ground-based telescopes, to provide simultaneous daily light curves of NGC 5548 across the X-ray, UV, and optical bands. For further details on the observational setup and data, we refer interested readers to De Rosa et al. (2015), Edelson et al. (2015), and Fausnaugh et al. (2016).

Applying EzTaoX to the UV/optical AGN STORM light curves of NGC 5548 reveals that the lags inferred by EzTaoX are broadly consistent with literature values derived using JAVELIN and ICCF. We follow the same strategy described in Section 3.1.2 to measure interband lags relative to the continuum light curve at 1367Å. In contrast to the approaches taken by Edelson et al. (2015), and Fausnaugh et al. (2016), we do not detrend the light curves prior to lag estimation. We also increased the prior range of $S_{\rm band}$ to Uniform(10^{-5} , 10) because AGN STORM light curve are provided in flux, which exhibits large amplitude variation across bands.

Figure 6 compares the lags measured with EzTaoX to those derived with JAVELIN and ICCF. F16 and E15 in the legend refer to the lags reported by Fausnaugh et al. (2016) and Edelson et al. (2015), respectively. The blue points represent the continuum lags measured at 1158Å, 1479Å, and 1746Å using HST light curves. The green points correspond to the continuum lags from the Swift UVW2, UVM2, UVW1, U, and B bands. The yellow points represent continuum lags from Johnson/Cousins BVRI bands and Sloan Digital Sky Survey (SDSS; York et al. 2000) ugriz bands based on ground-based observations. The purple squares in the right panel of Figure 6 shows the Swift lags reported by Edelson et al. (2015). We note that the Swift ICCF lags from Fausnaugh et al. (2016) are systematically larger than those reported by Edelson et al. (2015), likely due to the different de-trending approaches they adopted. Overall, interband lags measured using EzTaoX are broadly consistent with those obtained using JAVELIN and ICCF.

3.3. A Test Using Zwicky Transient Facility AGN Light Curves

The Zwicky Transient Facility (ZTF) is an optical time-domain survey that covers the entire sky north of $Dec = -30^{\circ}$ every $\sim 2-3$ nights in the gri bands (Bellm et al. 2019; Graham et al. 2019). The median 5σ depths

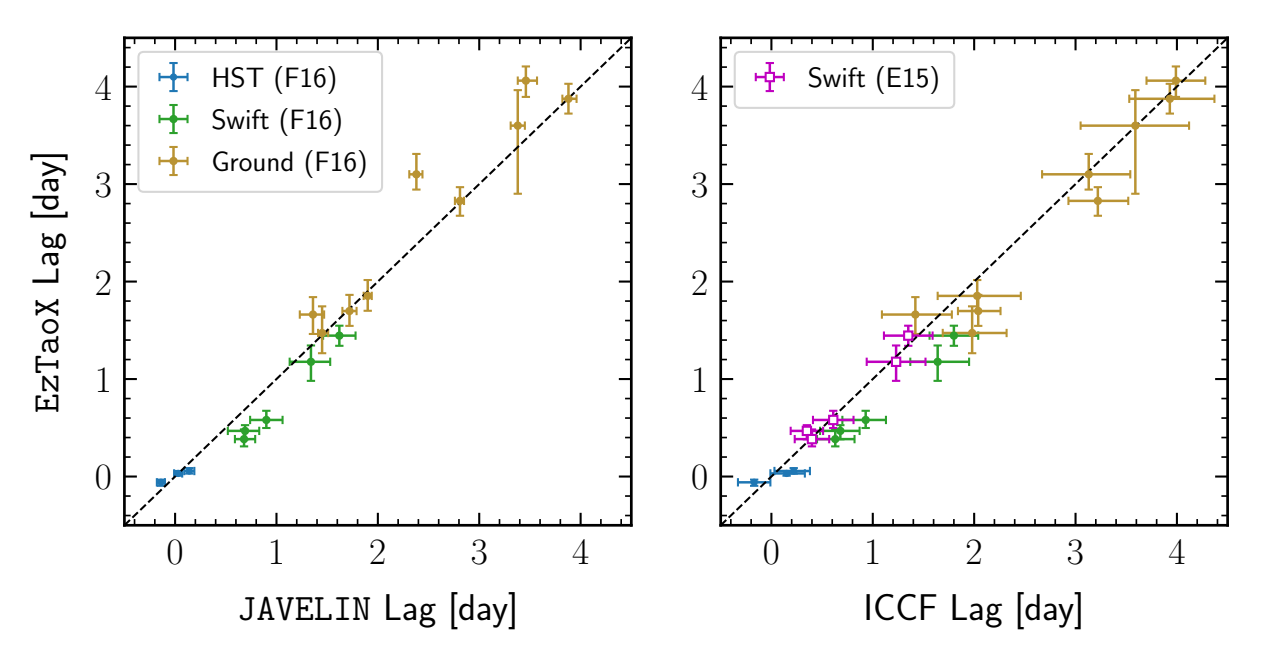


Figure 6. Comparison of interband continuum lags for NGC 5548 measured with EzTaoX to those reported in the literature. The light curves of NGC 5548 are obtained by the AGN STORM project. In the legend, F16 refers to the lags reported by Fausnaugh et al. (2016), and E15 refers to the lags reported by Edelson et al. (2015). Interband continuum lags measured with EzTaoX are broadly consistent with those obtained using JAVELIN and the ICCF method, highlighting the effectiveness of EzTaoX despite its adoption of a simplified transfer function (i.e., a Dirac delta function).

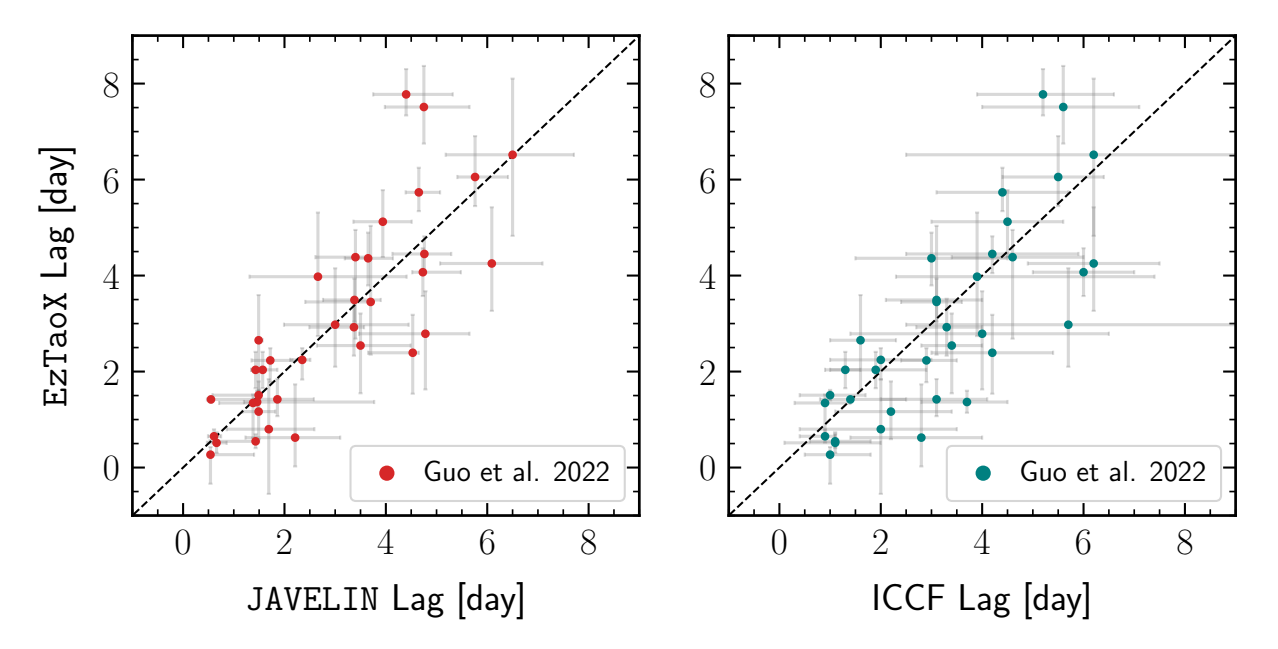


Figure 7. Comparison of interband continuum lags for a sample of type 1 AGNs measured with EzTaoX to those reported in the literature (Guo et al. 2022). The light curves are obtained from ZTF. Interband continuum lags measured with EzTaoX are broadly consistent with those obtained using JAVELIN (left) and the ICCF method (right)

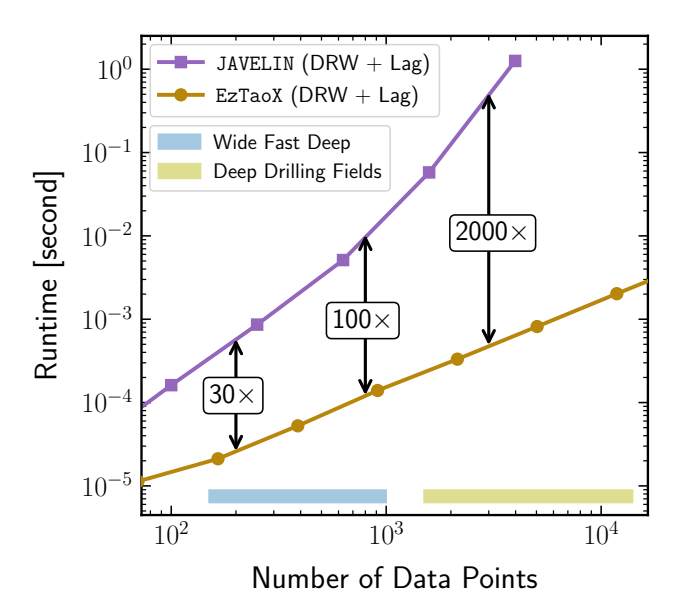


Figure 8. A computational benchmark comparison of EzTaoX and JAVELIN for evaluating the likelihood function of a light curve model that jointly estimates both the DRW parameters and the interband lag. The x-axis represents the total number of data points in a multiband light curve, while the y-axis indicates the corresponding computational cost for a single likelihood evaluation. The blue stripe near the bottom marks the parameter space corresponding to WFD light curves, ranging from $\sim\!200$ epochs in the g and r bands to $\sim\!800$ epochs across all six bands. The yellow stripe at the bottom marks the parameters space corresponding to DDF light curves. EzTaoX is $30{-}100\times$ faster than JAVELIN for WFD light curves and more than $2000\times$ faster for DDF light curves.

of ZTF reach $g\sim 20.8,\ r\sim 20.6$, and $i\sim 20.0$ mag (AB system) for a 30 s exposure (Masci et al. 2019). Using light curves from ZTF Data Release 7 (DR7), Guo et al. (2022) measured continuum lags for a large sample of type 1 AGNs at z<0.8, among which 38 objects (the "core" sample) have high-quality interband lag measurements from both JAVELIN and ICCF.

We apply EzTaoX to the g- and r-band ZTF light curves of the core-sample AGNs from Guo et al. (2022), and find that the lags measured with EzTaoX are broadly consistent with those obtained using JAVELIN and ICCF. Figure 7 compares the interband lags measured with EzTaoX to those from JAVELIN (left panel) and ICCF (right panel). We retrieve the ZTF light curves for these sources from the IPAC Infrared Science Archive (ZTF Team 2025) and truncate them to match the DR7 temporal baseline (i.e., MJD < 59400). When multiple light curves are available for the same object (each obtained from a different CCD), we select the one with the largest number of epochs. We follow the same strategy described in Section 3.1.2 to measure the lags between the

g and r bands. We also fit additional jitter terms—one for each band—added to the diagonal elements of the covariance matrix to account for any residual photometric uncertainties not captured by the photometric pipeline (Burke et al. 2021).

3.4. Scalability: Computation Time

For LSST light curves, EzTaoX is $\sim 10-10^3 \times \text{faster}$ than JAVELIN per likelihood evaluation. Figure 8 displays the computation time benchmarks for EzTaoX and JAVELIN, performed on an Apple Mac Mini with an M2 Pro chip, and the results reflect single-core CPU performance.⁵ For a typical 10-year q and r LSST WFD light curve—with ~ 60 g-band observations and ~ 170 rband observations (Ivezić et al. 2019)—EzTaoX achieves a reduction in computation time of $\sim 30 \times$ over JAVELIN. When light curves in all six bands are jointly modeled (assuming a total of 800 observations), the performance gain further increases to $\sim 100\times$. For a typical 10-year q and r LSST DDF light curve, which contains at least 10 times more observations in both the q and r bands, EzTaoX achieves a speed increase exceeding 2000×. The benchmark results are based on two-band light curves: however, the computational cost depends primarily on the total number of data points in the light curve. We suspect the observed speed increase primarily reflects the algorithmic advantages of celerite; however, without the JIT compilation provided by JAX, EzTaoX would be $\sim 5-10\times$ slower for WFD light curves.

An additional increase in speed of up to $10 \times$ can be achieved by using more efficient sampling algorithms/tools. Upon obtaining a point estimate of the model parameters through optimizing the likelihood function, uncertainties on model parameters can be quantified through posterior sampling, typically performed using MCMC methods. Most existing AGN light curve modeling tools adopt emcee for MCMC sampling, which is adequate for most inference tasks. However, emcee can become computationally inefficient when nontrivial or computationally intensive prior distributions are introduced. NumPyro⁶—a probabilistic programming library built on JAX—overcomes this limitation by compiling custom prior distribution functions at runtime using JIT compilation, thereby enabling more efficient posterior sampling (Phan et al. 2019; Bingham et al. 2019). NumPyro provides efficient implementations of various MCMC algorithms, including the affine-invariant en-

We also benchmarked EzTaoX under multi-core settings (i.e., each core running an independent benchmarking job in parallel), and the resulting performance remained unchanged.

⁶ https://github.com/pyro-ppl/numpyro

semble sampler implemented in emcee and NUTS. In our tests, NUTS implemented in NumPyro achieves up to a tenfold speed increase over emcee in generating 5000 effective posterior samples $(n_{\rm eff})$, when applied to the same set of two-band light curves and using identical prior distributions for EzTaoX parameters.

4. DISCUSSION

4.1. Unbiased Point Estimator of τ_{DRW}

Unbiased recovery of $\tau_{\rm DRW}$ depends on the light-curve cadence, baseline (i.e., the total duration of observations), and adopted priors. As shown by Kozłowski (2017) and later studies (e.g., Sánchez-Sáez et al. 2018; Burke et al. 2021; Suberlak et al. 2021; Hu et al. 2024), $\tau_{\rm DRW}$ is systematically underestimated when the light-curve baseline is shorter than ~10 times the true $\tau_{\rm DRW}$. Hu et al. (2024) conducted extensive simulations demonstrating that the assumed prior on $\tau_{\rm DRW}$ also impact its recovery. In addition, they reported that $\tau_{\rm DRW}$ is systematically overestimated when the true $\tau_{\rm DRW}$ is less than five times the mean cadence, since the temporal sampling then probes only the white-noise regime (i.e., a PL exponent of zero) of the DRW PSD.

Following previous investigations, we perform simulations to assess how accurately EzTaoX recovers $\tau_{\rm DRW}$ as a function of $\tau_{\rm DRW}$ -to-baseline ratio. We simulated 5000 single-band light curves with a uniform 2-day cadence and a baseline of 10^4 days. Each light curve adopts a fiducial $\sigma_{\rm DRW}$ of 0.112 mag and a mean photometric uncertainty of 0.01 mag. The input $\tau_{\rm DRW}$ ranges from 10 days to 10^4 days, corresponding to an input $\tau_{\rm DRW}$ -to-baseline ratios ($\rho_{\rm in}$) spanning from 0.001 to 1. We fit the simulated single-band light curves using EzTaoX to infer $\tau_{\rm DRW}$ and $\sigma_{\rm DRW}$, following the strategy outlined in Section 3.1.2. To avoid potential prior-driven biases, we extend the upper limit of the MCMC prior on $\tau_{\rm DRW}$ to 10^5 days—an order of magnitude longer than the light-curve baseline.

Based on our simulations, EzTaoX recovers $\tau_{\rm DRW}$ without systematic bias up to one tenth of the light-curve baseline. Figure 9 displays the distribution of $\Delta \log(\tau_{\rm DRW})$ —the difference between the recovered and input $\log(\tau_{\rm DRW})$ —as a function of the recovered $\tau_{\rm DRW}$ to-baseline ratio ($\rho_{\rm out}$). Plotting $\rho_{\rm out}$ rather than $\rho_{\rm in}$ is more informative, since the true $\tau_{\rm DRW}$ is unknown when fitting DRW models to real AGN light curves. In each panel, the dash-dotted line indicates the median of the $\Delta \log(\tau_{\rm DRW})$ distribution, and the shaded region shows its central 68% interval. The top, middle, and bottom panels correspond to three common point estimators: MLE, MCMC posterior median, and MCMC posterior mean, respectively. Among these, the MCMC

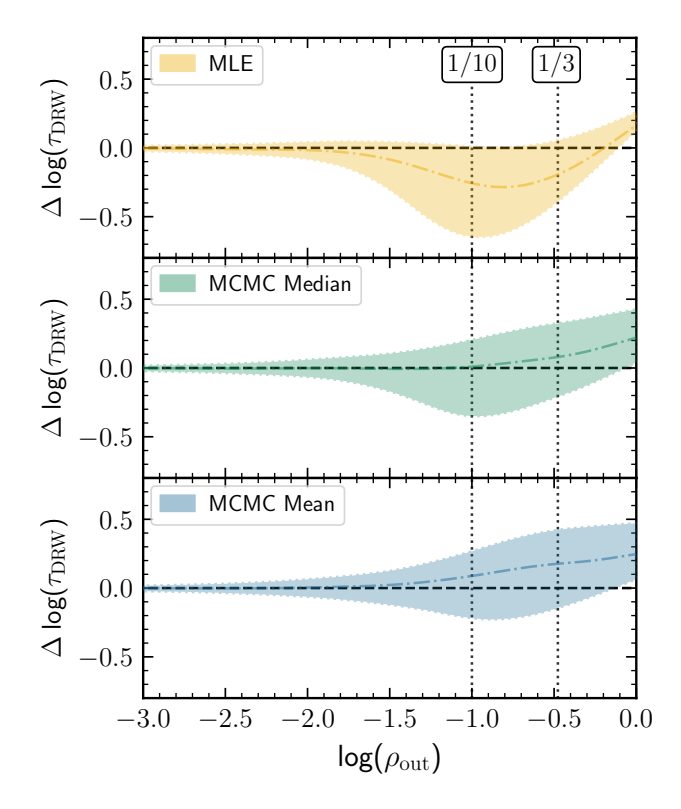


Figure 9. Comparison of three point estimators for τ_{DRW} : MLE, MCMC posterior median, and MCMC posterior mean. The x-axis is the recovered τ_{DRW} -to-baseline ratio (ρ_{out}), and the y-axis is the difference between the recovered and true values of $\log(\tau_{\text{DRW}})$. In each panel, the dash-dotted line marks the median of the $\Delta\log(\tau_{\text{DRW}})$ distribution, and the shaded region shows its central 68% interval. The MCMC posterior median is the most reliable, yielding systematically unbiased estimates up to one tenth of the light-curve baseline (vertical dotted line, left) and introducing only a small systematic bias of ~ 0.1 dex at one third of the baseline (vertical dotted line, right).

posterior median is the most robust, remaining systematically unbiased as long as the the recovered $\tau_{\rm DRW}$ is less than one-tenth of the baseline (dash-dotted lines in the middle panel of Figure 9). It introduces only a small systematic bias (~ 0.1 dex) when the recovered $\tau_{\rm DRW}$ is about one-third of the baseline.

4.2. Deviation from DRW

In this work, we assume that AGN stochastic variability follows a DRW process; however, the modeling framework introduced here is sufficiently flexible to accommodate alternative GP kernels for characterizing the underlying variability. As an illustration, Figure 10 presents g- and r-band light curves simulated using a CARMA(2,1) process, sampled according to the LSST WFD cadence (left), along with the corresponding PSDs recovered using EzTaoX (right). The CARMA(2,1)

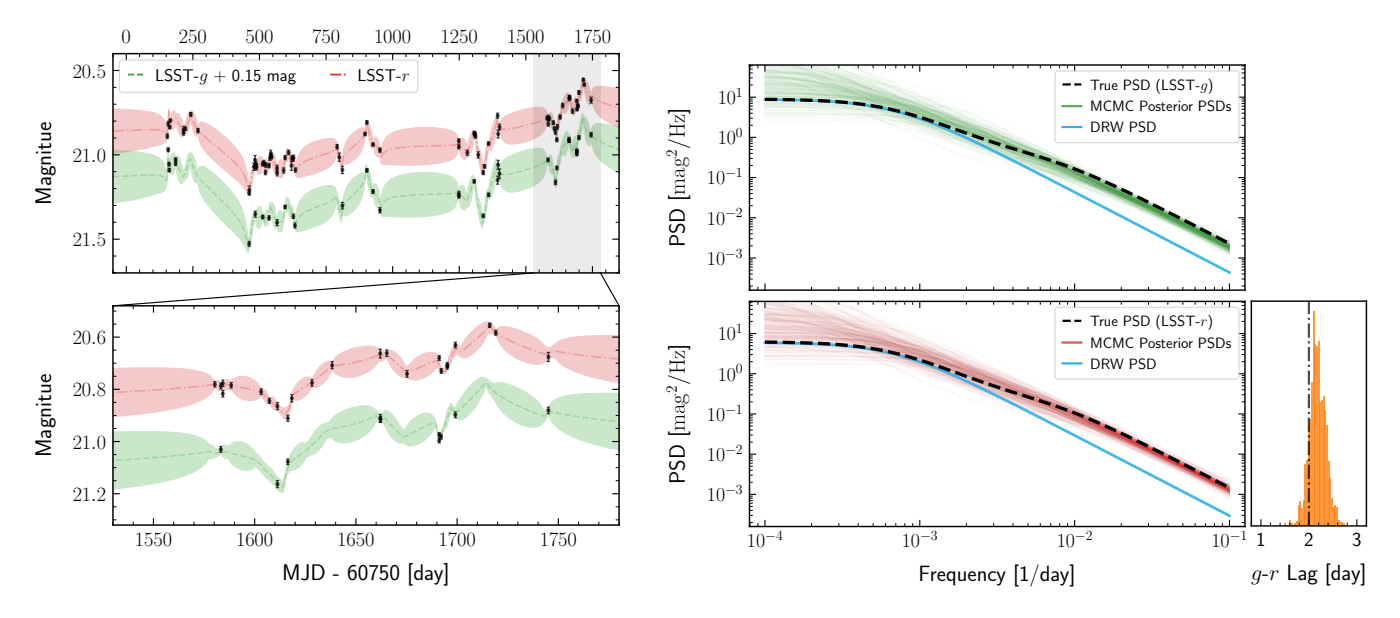


Figure 10. Left: Example LSST WFD light curves simulated using a CARMA(2,1) model. The g- and r-band light curves have fiducial mean magnitudes of 21 and 20.9, respectively. Right: The true (dashed curves) and recovered (colored solid curves) PSDs. The recovered PSDs are generated using random draws of the MCMC posterior distribution. As a comparison, the blue dashed curves display the reference DRW PSDs. The orange histogram in the bottom right panel shows the posterior distribution of the recovered g-r lag, with the dash-dotted vertical line indicating the true simulated lag of 2 days.

process—also known as the noise-driven damped harmonic oscillator (DHO) model—has been shown to provide superior fits to observed AGN UV/optical light curves compared to the DRW model (e.g., Kasliwal et al. 2017; Yu et al. 2025). For reference, the DRW PSD is shown in blue in the right panel. Similar to Figure 1, the orange histogram in the lower right corner displays the posterior distribution of the g-r lag. The specific CARMA(2,1) process simulated is governed by the following kernel:

$$k(t_i, t_j) = a_1 e^{-c_1 |t_j - t_i|} + a_2 e^{-c_2 |t_j - t_i|},$$
 (9)

which is equivalent to the sum of two DRW kernels.

4.3. Beyond the Dirac Delta Transfer Function

EzTaoX models interband lags in multiband light curves using a Dirac delta transfer function, a simplified approach compared to methods that adopt more flexible transfer functions with finite width and skewed shapes (e.g., Zu et al. 2011; Starkey et al. 2016; Li et al. 2016; Donnan et al. 2021). While more sophisticated transfer functions can provide additional insights into the geometry and physical properties of AGN accretion disks (e.g., Cackett et al. 2007; Starkey et al. 2016; Fagin et al. 2024), we argue that the cadence of LSST WFD light curves is likely insufficient to resolve the detailed shape of the transfer functions. Thus, the simplified Dirac delta transfer function adopted by EzTaoX is likely adequate for lag estimation from LSST WFD light

curves. Furthermore, previous investigations and the results of Section 3.2 show that even with high-cadence continuum reverberation mapping data, the use of more flexible transfer functions does not necessarily result in significantly different mean lag estimates compared to simpler methods (e.g., Fausnaugh et al. 2018; Donnan et al. 2023). An exception perhaps arises when the intrinsic transfer function is notably skewed, in which case simplified methods may underestimate the mean lag (Yu et al. 2020a; Chan et al. 2020).

As an extension to the comparison in Section 3.1.2, we test EzTaoX and JAVELIN on new sets of 10-year LSST WFD light curves simulated with a Gaussian transfer function. As before, the g-band light curves adopt an input $\tau_{\rm DRW} = 100$ days and $\sigma_{\rm DRW} = 0.112$ mag. The r-band light curves are generated by convolving the q-band curves with a Gaussian transfer function. We simulate three sets of light curves with fixed Gaussian widths of 0.5, 2, and 5 days. Following the same procedure as in Section 3.1.2, we extract q-r lags from the simulated light curves using both EzTaoX and JAVELIN; the results are shown in Figure 11. We find that EzTaoX yields lag measurements comparable to those of JAVELIN even when the transfer function width is as large as 5 days. Moreover, the n_{eff} -based sample cleaning procedure tends to removes a higher fraction of EzTaoX fits with true lags much smaller than the transfer function width, while preferentially discarding JAVELIN fits with true lags much larger than the width. This behavior explains the trend noted in Section 3.1.2,

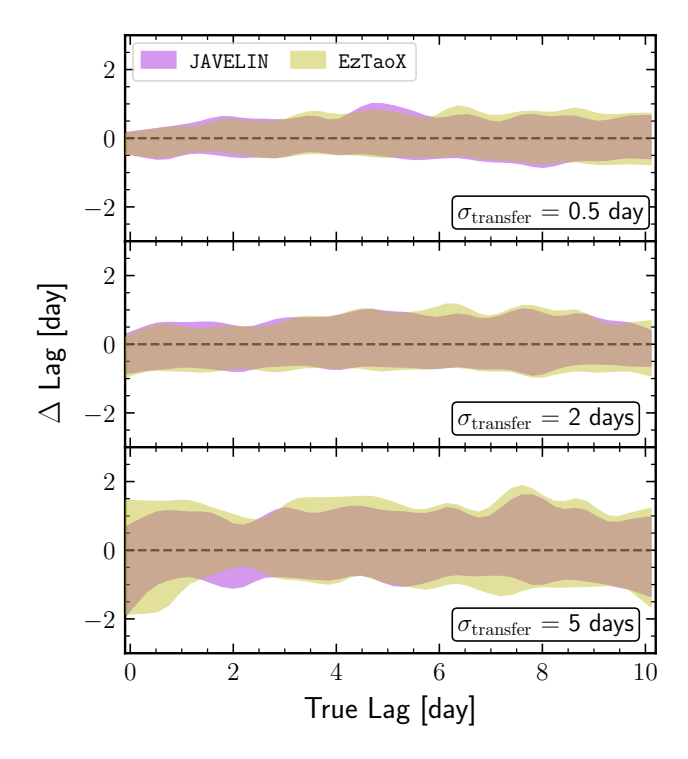


Figure 11. Comparisons of g–r lags extracted by EzTaoX and JAVELIN from 10-year LSST WFD light curves simulated with Gaussian transfer functions of width 0.5, 2, and 5 days (top to bottom). The shaded regions shows the central 68% interval of the Δ lag distribution. EzTaoX yields lag measurements comparable to those of JAVELIN, even when the light curves are simulated with a transfer function width as wide as 5 days.

where the fraction of discarded JAVELIN fits increases with true lag when the light curves are simulated with a Dirac delta transfer function.

4.4. LSST Variability Science Enabled by EzTaoX

EzTaoX enables reliable and simultaneous characterization of variability and interband lags for the tens of millions of AGNs to be monitored by LSST. Existing non-ML methods/tools capable of jointly characterizing stochastic variability and measuring interband lags are not scalable to LSST data volumes (e.g., Zu et al. 2011; Starkey et al. 2016; Donnan et al. 2021). While ML approaches are scalable, their reliability critically depends on the assumption that the training data accurately capture the true nature of AGN variability—an assumption that is rarely satisfied in practice. In comparison to traditional non-ML tools, EzTaoX achieves a speed increase of $> 100 \times$ for LSST WFD light curves, and $> 10^4 \times$ for LSST DDF light curves, without compromising—and in some cases improving—the accuracy of the results. Furthermore, EzTaoX offers the flexibility to incorporate more expressive GP kernels, allowing

for improved modeling of intrinsic continuum variability. This combination of scalability and flexibility enables robust characterization of variability and interband lags for an unprecedented number of AGNs. A large, statistically significant sample of AGNs with well-characterized continuum variability and interband lags will facilitate detailed investigations into the fundamental drivers of AGN variability and the physical origins of continuum lags.

EzTaoX enables robust variability selection of actively accreting MBHs. Accreting MBHs in dwarf galaxies are difficult to identify due to their low luminosity relative to their host galaxy starlight (Greene et al. 2020). Nevertheless, their characteristic stochastic variability provides a powerful selection tool in the time domain (e.g., Baldassare et al. 2018; Ward et al. 2022; Burke et al. 2022; Bernal et al. 2025). By modeling dwarf galaxy image-differencing light curves as a DRW process, one can identify MBH candidates, which are expected to exhibit characteristic τ_{DRW} values ranging from hours to days (Burke et al. 2021; Wang et al. 2023). Given the cadence of LSST WFD light curves, the multiband modeling capability of EzTaoX enables precise measurement of τ_{DRW} on timescales from one hour to one day (see Figure 3), outperforming single-band approaches. When nightly stacked images are required to detect variability from fainter sources, the intra-night cadence in single-band LSST light curves is lost, leading to biased τ_{DRW} estimates (see Figure 4). In contrast, through multiband fitting, EzTaoX recovers τ_{DRW} without bias down to hourly timescales for AGNs detected in the WFD survey.

4.5. Caveats & Future Work

Variable emission from extended re-processors is not explicitly modeled in the current implementation of EzTaoX. Recent investigations suggest that reprocessed emission arising at distances much larger than the scale of the accretion disk—for example, in the BLR—can contribute to the measured continuum lags, potentially leading to overestimated accretion disk sizes relative to theoretical predictions (e.g., Korista & Goad 2001; McHardy et al. 2018; Cackett et al. 2018; Lawther et al. 2018; Lira et al. 2024; Jaiswal et al. 2024; Leighly et al. 2024). The current multiband light curve model in EzTaoX assumes a single lag between any two photometric bands, and therefore lacks the capacity to disentangle multi-component lag distributions, such as reprocessed emission arising from the accretion disk versus that from much larger scales. Developing methodologies that can decompose observed light curves into distinct lagged components would be highly valuable—not

only for probing the detailed geometry of AGN accretion flows, but also for advancing our understanding of the physical drivers behind AGN stochastic variability.

The GP kernels currently supported by EzTaoX are all stationary; however, AGN stochastic variability may exhibit non-stationary behavior. A notable example is the class of changing-look AGNs (see Ricci & Trakhtenbrot 2023 and references therein), which exhibit dramatic variability on the timescale of years to decades, likely driven by extreme changes in the accretion rate of the disk (e.g., Ruan et al. 2016; Noda & Done 2018; Graham et al. 2020; Panda & Śniegowska 2024). Such systems underscore the limitations of assuming stationarity in modeling AGN variability. Future development of EzTaoX will explore non-stationary GP kernels, in which the kernel parameters evolve with time rather than remaining fixed (e.g., Noack & Sethian 2021).

5. SUMMARY & CONCLUSION

We present EzTaoX —a new software package designed to leverage multiband AGN light curves for joint inference of intrinsic stochastic variability properties and interband continuum lags. We evaluate the performance of EzTaoX using both simulated LSST AGN light curves sampled at the cadence of the WFD survey, and multiwavelength light curves of real AGNs. The EzTaoX software is available on GitHub⁷ under a MIT License and version 0.1 is archived in Zenodo (Yu & Burke 2025). The key advancements and capabilities of EzTaoX are summarized as follows:

- EzTaoX is $\sim 10^2 10^3$ times faster than JAVELIN for LSST WFD light curves, and more than $\sim 10^4 \times$ faster for DDF light curves (see Figure 8 and Section 3.4).
- EzTaoX and JAVELIN show comparable reliability in recovering simulated interband lags. Specifically, lags can be recovered to within ~ 2 days (1σ) using the first 3 years of LSST WFD observations (assuming a fiducial $\tau_{\rm DRW}$ of 100 days, a $\sigma_{\rm DRW}$ of 0.112 mag, and a g-band mean magnitude of 21), and to within ~ 0.7 day (1σ) with the full 10-year dataset (see Figure 2).
- EzTaoX provides more reliable recovery of the simulated τ_{DRW} and σ_{DRW} than JAVELIN. In particular, JAVELIN produces systematically biased estimates, whereas EzTaoX recovers unbiased results across the tested range (see Figure 3 and Figure 5).

- EzTaoX's multiband modeling capability enables robust recovery of τ_{DRW} down to hourly timescales with simulated LSST WFD light curves, outperforming single-band modeling. This precision enhances the ability to identify low-mass AGNs (e.g., those in dwarf galaxies) through variability (see Figure 4).
- EzTaoX supports a broad class of GP kernels beyond the DRW model for joint modeling of AGN stochastic variability and interband lags, offering greater modeling flexibility (see Figure 10 for an example).

In addition to characterizing AGN stochastic variability and measuring continuum lags, EzTaoX is applicable to a variety of other time-domain astrophysical studies. For example, EzTaoX can be applied to measure BLR emission line lags from spectroscopic RM light curves (Blandford & McKee 1982), or to detect negative lags that may arise from inward propagation of accretion rate fluctuations (Secunda et al. 2023)—both of which typically occur on timescales much longer than the continuum lags. Moreover, EzTaoX can be used to measure time delays between the multiple images of gravitationally lensed quasars, providing an important avenue for constraining the Hubble constant (Blandford & Narayan 1992). Finally, interband lags have been shown to correlate with AGN continuum luminosity (e.g., Sergeev et al. 2005; Netzer 2021; Guo et al. 2022; Panda et al. 2024); once properly calibrated, this lag-luminosity relation may enable the estimation of AGN physical properties using photometric time-domain data alone.

We thank Maurizio Paolillo for providing comments to an early draft of this manuscript. W.Y. acknowledges support from the Dunlap Institute for Astronomy & Astrophysics at the University of Toronto. J.J.R. acknowledges support from the Canada Research Chairs (CRC) program, the NSERC Discovery Grant program, the Canada Foundation for Innovation (CFI), and the Québec Ministère de l'Économie et de l'Innovation. C.J.B. is supported by an NSF Astronomy and Astrophysics Postdoctoral Fellowship under award AST-2303803. This material is based upon work supported by the National Science Foundation under Award No. This research award to NSF is partially funded by a generous gift of Charles Simonyi to the NSF Division of Astronomical Sciences. The award is made in recognition of significant contributions to Rubin Observatory's Legacy Survey of Space and Time. R.J.A., F.E.B, and S.S.S. gratefully acknowledge sup-

⁷ EzTaoX codebase: https://github.com/ywx649999311/EzTaoX.

port from ANID: CATA BASAL FB210003 (R.J.A., F.E.B., S.S.S.); Millennium Science Initiative AIM23-0001 (F.E.B.); and FONDECYT Regular 1231718 (R.J.A.) and 1241005 (F.E.B.). D.D. acknowledges PON R&I 2021, CUP E65F21002880003, and Fondi di Ricerca di Ateneo (FRA), linea C, progetto TORNADO. L.H.G. acknowledges financial support from ANID programs: FONDECYT Iniciación 11241477, Millennium Science Initiative Programs NCN2023-002, and AIM23-0001. D.I. and A.B.K. acknowledge funding provided by the University of Belgrade - Faculty of Mathematics (the contract 451-03-136/2025-03/200104) through the grant by the Ministry of Science, Technological Development and Innovation of the Republic of Serbia. S.P. is supported by the international Gemini Observatory, a program of NSF NOIRLab, which is managed by the Association of Universities for Research in Astronomy (AURA) under a cooperative agreement with the U.S. National Science Foundation, on behalf of the Gemini partnership of Argentina, Brazil, Canada, Chile, the Republic of Korea, and the United States of America.

Based on observations obtained with the Samuel Oschin Telescope 48-inch and the 60-inch Telescope at

the Palomar Observatory as part of the Zwicky Transient Facility project. ZTF is supported by the National Science Foundation under Grants No. AST-1440341 and AST-2034437 and a collaboration including current partners Caltech, IPAC, the Oskar Klein Center at Stockholm University, the University of Maryland, University of California, Berkeley, the University of Wisconsin at Milwaukee, University of Warwick, Ruhr University, Cornell University, Northwestern University and Drexel University. Operations are conducted by COO, IPAC, and UW.

Software: pandas (McKinney 2010), numpy (Harris et al. 2020), scipy (Virtanen et al. 2020), matplotlib (Hunter 2007), astropy (The Astropy Collaboration et al. 2013; The Astropy Collaboration et al. 2018; Astropy Collaboration et al. 2022), emcee (Foreman-Mackey et al. 2013), eztao (Yu & Richards 2022), tinygp (Foreman-Mackey et al. 2024), numpyro (Bingham et al. 2019; Phan et al. 2019) eztaox (Yu & Burke 2025)

REFERENCES

Aigrain, S., & Foreman-Mackey, D. 2023, ARA&A, 61, 329, doi: 10.1146/annurev-astro-052920-103508

Alexander, T. 1997, in Astrophysics and Space Science Library, Vol. 218, Astronomical Time Series, ed.
D. Maoz, A. Sternberg, & E. M. Leibowitz, 163, doi: 10.1007/978-94-015-8941-3 14

Arévalo, P., Churazov, E., Lira, P., et al. 2024, A&A, 684, A133, doi: 10.1051/0004-6361/202347080

Astropy Collaboration, Price-Whelan, A. M., Lim, P. L., et al. 2022, ApJ, 935, 167, doi: 10.3847/1538-4357/ac7c74

Baldassare, V. F., Geha, M., & Greene, J. 2018, ApJ, 868, 152, doi: 10.3847/1538-4357/aae6cf

Baldassare, V. F., Reines, A. E., Gallo, E., & Greene, J. E. 2017, ApJ, 836, 20, doi: 10.3847/1538-4357/836/1/20

Beard, M. W. J., McHardy, I. M., Horne, K., et al. 2025, MNRAS, 537, 293, doi: 10.1093/mnras/staf014

Bellm, E. C., Kulkarni, S. R., Graham, M. J., et al. 2019, PASP, 131, 018002, doi: 10.1088/1538-3873/aaecbe

Bernal, S., Sánchez-Sáez, P., Arévalo, P., et al. 2025, A&A, 694, A127, doi: 10.1051/0004-6361/202451870

Bingham, E., Chen, J. P., Jankowiak, M., et al. 2019, J. Mach. Learn. Res., 20, 28:1.

http://jmlr.org/papers/v20/18-403.html

Blandford, R. D., & McKee, C. F. 1982, ApJ, 255, 419, doi: 10.1086/159843 Blandford, R. D., & Narayan, R. 1992, ARA&A, 30, 311, doi: 10.1146/annurev.astro.30.1.311

Brandt, W. N., Ni, Q., Yang, G., et al. 2018, arXiv:1811.06542 [astro-ph]. https://arxiv.org/abs/1811.06542

Burke, C. J., Shen, Y., Blaes, O., et al. 2021, Sci, 373, 789, doi: 10.1126/science.abg9933

Burke, C. J., Liu, X., Shen, Y., et al. 2022, MNRAS, 516, 2736, doi: 10.1093/mnras/stac2262

Butler, N. R., & Bloom, J. S. 2011, AJ, 141, doi: 10.1088/0004-6256/141/3/93

Cackett, E. M., Bentz, M. C., & Kara, E. 2021, iScience, 24, 102557, doi: 10.1016/j.isci.2021.102557

Cackett, E. M., Chiang, C.-Y., McHardy, I., et al. 2018, ApJ, 857, 53, doi: 10.3847/1538-4357/aab4f7

Cackett, E. M., Horne, K., & Winkler, H. 2007, MNRAS, 380, 669, doi: 10.1111/j.1365-2966.2007.12098.x

Chan, J. H. H., Millon, M., Bonvin, V., & Courbin, F. 2020, A&A, 636, A52, doi: 10.1051/0004-6361/201935423

Collier, S., Horne, K., Wanders, I., & Peterson, B. M. 1999, MNRAS, 302, L24, doi: 10.1046/j.1365-8711.1999.02250.x

Collier, S. J., Horne, K., Kaspi, S., et al. 1998, ApJ, 500, 162, doi: 10.1086/305720

Cornachione, M. A., Morgan, C. W., Millon, M., et al. 2020, ApJ, 895, 125, doi: 10.3847/1538-4357/ab557a

- Cranmer, K., Brehmer, J., & Louppe, G. 2020, Proc Natl Acad Sci USA, 201912789, doi: 10.1073/pnas.1912789117
- Dai, X., Kochanek, C. S., Chartas, G., et al. 2010, ApJ, 709, 278, doi: 10.1088/0004-637X/709/1/278
- De Cicco, D., Bauer, F. E., Paolillo, M., et al. 2021, A&A, 645, A103, doi: 10.1051/0004-6361/202039193
- De Cicco, D., Bauer, F. E., Paolillo, M., et al. 2022, A&A, 664, A117, doi: 10.1051/0004-6361/202142750
- De Rosa, G., Peterson, B. M., Ely, J., et al. 2015, ApJ, 806, 128, doi: 10.1088/0004-637X/806/1/128
- Dexter, J., & Agol, E. 2011, ApJ, 727, L24, doi: 10.1088/2041-8205/727/1/L24
- Donnan, F. R., Horne, K., & Hernández Santisteban, J. V. 2021, MNRAS, 508, 5449, doi: 10.1093/mnras/stab2832
- Donnan, F. R., Hernández Santisteban, J. V., Horne, K., et al. 2023, MNRAS, 523, 545, doi: 10.1093/mnras/stad1409
- Edelson, R., Gelbord, J. M., Horne, K., et al. 2015, ApJ, 806, 129, doi: 10.1088/0004-637X/806/1/129
- Edelson, R. A., & Krolik, J. H. 1988, ApJ, 333, 646, doi: 10.1086/166773
- Fagin, J., Park, J. W., Best, H., et al. 2024, ApJ, 965, 104, doi: 10.3847/1538-4357/ad2988
- Fausnaugh, M. M., Denney, K. D., Barth, A. J., et al. 2016, ApJ, 821, 56, doi: 10.3847/0004-637X/821/1/56
- Fausnaugh, M. M., Starkey, D. A., Horne, K., et al. 2018, ApJ, 854, 107, doi: 10.3847/1538-4357/aaaa2b
- Foreman-Mackey, D., Agol, E., Ambikasaran, S., & Angus, R. 2017, AJ, 154, 220, doi: 10.3847/1538-3881/aa9332
- Foreman-Mackey, D., Hogg, D. W., Lang, D., & Goodman, J. 2013, PASP, 125, 306, doi: 10.1086/670067
- Foreman-Mackey, D., Yu, W., Yadav, S., et al. 2024, Zenodo, doi: 10.5281/zenodo.10463641
- Gaskell, C. M. 2004, ApJ, 612, L21, doi: 10.1086/424565
- Gaskell, C. M., & Peterson, B. M. 1987, ApJS, 65, 1, doi: 10.1086/191216
- Gehrels, N., Chincarini, G., Giommi, P., et al. 2004, ApJ, 611, 1005, doi: 10.1086/422091
- Giebels, B., & Degrange, B. 2009, A&A, 503, 797, doi: 10.1051/0004-6361/200912303
- Goodman, J., & Weare, J. 2010, CAMCoS, 5, 65, doi: 10.2140/camcos.2010.5.65
- Gordon, T. A., Agol, E., & Foreman-Mackey, D. 2020, AJ, 160, 240, doi: 10.3847/1538-3881/abbc16
- Graham, M. J., Kulkarni, S. R., Bellm, E. C., et al. 2019, PASP, 131, 078001, doi: 10.1088/1538-3873/ab006c
- Graham, M. J., Ross, N. P., Stern, D., et al. 2020, MNRAS, 491, 4925, doi: 10.1093/mnras/stz3244
- Greene, J. E., Strader, J., & Ho, L. C. 2020, ARA&A, 58, 257, doi: 10.1146/annurev-astro-032620-021835

- Griffiths, R.-R., Jiang, J., Buisson, D. J. K., et al. 2021, ApJ, 914, 144, doi: 10.3847/1538-4357/abfa9f
- Guo, H., Barth, A. J., & Wang, S. 2022, ApJ, 940, 20, doi: 10.3847/1538-4357/ac96ec
- Gúrpide, A., & Middleton, M. 2025, MNRAS, 537, 3210, doi: 10.1093/mnras/staf196
- Harris, C. R., Millman, K. J., van der Walt, S. J., et al. 2020, Natur, 585, 357, doi: 10.1038/s41586-020-2649-2
- Hoffman, M. D., & Gelman, A. 2011, arXiv e-prints, arXiv:1111.4246, doi: 10.48550/arXiv.1111.4246
- Homayouni, Y., Trump, J. R., Grier, C. J., et al. 2019, ApJ, 880, 126, doi: 10.3847/1538-4357/ab2638
- Hu, X.-F., Cai, Z.-Y., & Wang, J.-X. 2024, ApJ, 961, 5, doi: 10.3847/1538-4357/ad072f
- Hunter, J. D. 2007, Comput. Sci. Eng., 9, 90, doi: 10.1109/MCSE.2007.55
- Ivezić, Ž., Kahn, S. M., Tyson, J. A., et al. 2019, ApJ, 873, 111, doi: 10.3847/1538-4357/ab042c
- Jaiswal, V. K., Mandal, A. K., Prince, R., et al. 2024, arXiv e-prints, arXiv:2410.03597, doi: 10.48550/arXiv.2410.03597
- Jha, V. K., Joshi, R., Chand, H., et al. 2022, MNRAS, 511, 3005, doi: 10.1093/mnras/stac109
- Jiang, Y.-F., Green, P. J., Greene, J. E., et al. 2017, ApJ, 836, 186, doi: 10.3847/1538-4357/aa5b91
- Jiménez-Vicente, J., Mediavilla, E., Kochanek, C. S., et al. 2014, ApJ, 783, 47, doi: 10.1088/0004-637X/783/1/47
- Kammoun, E. S., Papadakis, I. E., & Dovčiak, M. 2021, MNRAS, 503, 4163, doi: 10.1093/mnras/stab725
- $\label{eq:Kasliwal} Kasliwal, V. P., Vogeley, M. S., \& Richards, G. T. 2015, \\ MNRAS, 451, 4328, doi: <math>10.1093/mnras/stv1230$
- —. 2017, MNRAS, 470, 3027, doi: 10.1093/mnras/stx1420
- Kelly, B. C., Bechtold, J., & Siemiginowska, A. 2009, ApJ, 698, 895, doi: 10.1088/0004-637X/698/1/895
- Kelly, B. C., Becker, A. C., Sobolewska, M., Siemiginowska, A., & Uttley, P. 2014, ApJ, 788, doi: 10.1088/0004-637X/788/1/33
- Korista, K. T., & Goad, M. R. 2001, ApJ, 553, 695, doi: 10.1086/320964
- Kovačević, A. B., Radović, V., Ilić, D., et al. 2022, ApJS, 262, 49, doi: 10.3847/1538-4365/ac88ce
- Kozłowski, S. 2016, ApJ, 826,
 - doi: 10.3847/0004-637X/826/2/118
- —. 2017, A&A, 597, 128,doi: 10.1051/0004-6361/201629890
- Kozłowski, S., Kochanek, C. S., Udalski, A., et al. 2010, ApJ, 708, 927, doi: 10.1088/0004-637X/708/2/927
- Krolik, J. H., Horne, K., Kallman, T. R., et al. 1991, ApJ, 371, 541, doi: 10.1086/169918

- Lawther, D., Goad, M. R., Korista, K. T., Ulrich, O., & Vestergaard, M. 2018, MNRAS, 481, 533, doi: 10.1093/mnras/sty2242
- Lefkir, M., Vaughan, S., Huppenkothen, D., Uttley, P., & Anilkumar, V. 2025, MNRAS, 539, 1775, doi: 10.1093/mnras/staf532
- Leighly, K. M., Choi, H., Eracleous, M., et al. 2024, ApJ, 966, 87, doi: 10.3847/1538-4357/ad2f2a
- Li, J. I.-H., Johnson, S. D., Avestruz, C., et al. 2024, ApJ, 977, 223, doi: 10.3847/1538-4357/ad900d
- Li, Y.-R., Wang, J.-M., & Bai, J.-M. 2016, ApJ, 831, 206, doi: 10.3847/0004-637X/831/2/206
- Lira, P., Sánchez-Sáez, P., Arévalo, P., et al. 2024, MNRAS, 531, 3310, doi: 10.1093/mnras/stae1095
- Lyubarskii, Yu. E. 1997, MNRAS, 292, 679, doi: 10.1093/mnras/292.3.679
- MacLeod, C. L., Ivezić, Ž., Kochanek, C. S., et al. 2010, ApJ, 721, 1014, doi: 10.1088/0004-637X/721/2/1014
- MacLeod, C. L., Brooks, K., Ivezić, Ž., et al. 2011, ApJ, 728, doi: 10.1088/0004-637X/728/1/26
- MacLeod, C. L., Ivezić, Ž., Sesar, B., et al. 2012, ApJ, 753, 106, doi: 10.1088/0004-637X/753/2/106
- Marshall, P., Anguita, T., Bianco, F. B., et al. 2017, doi: 10.5281/zenodo.842713
- Masci, F. J., Laher, R. R., Rusholme, B., et al. 2019, PASP, 131, 018003, doi: 10.1088/1538-3873/aae8ac
- McHardy, I. M., Connolly, S. D., Horne, K., et al. 2018, MNRAS, 480, 2881, doi: 10.1093/mnras/sty1983
- McKinney, W. 2010, in Python in Science Conference, Austin, Texas, 56–61, doi: 10.25080/Majora-92bf1922-00a
- McLaughlin, S. A. J., Mullaney, J. R., & Littlefair, S. P. 2024, MNRAS, 529, 2877, doi: 10.1093/mnras/stae721
- Moreno, J., Vogeley, M. S., Richards, G. T., & Yu, W. 2019, PASP, 131, 063001, doi: 10.1088/1538-3873/ab1597
- Morgan, C. W., Kochanek, C. S., Morgan, N. D., & Falco,
 E. E. 2010, ApJ, 712, 1129,
 doi: 10.1088/0004-637X/712/2/1129
- Mudd, D., Martini, P., Zu, Y., et al. 2018, ApJ, 862, 123, doi: 10.3847/1538-4357/aac9bb
- Mushotzky, R. F., Edelson, R., Baumgartner, W., & Gandhi, P. 2011, ApJ, 743, L12, doi: 10.1088/2041-8205/743/1/L12
- Netzer, H. 2021, MNRAS, stab3133, doi: 10.1093/mnras/stab3133
- Noack, M. M., & Sethian, J. A. 2021, arXiv e-prints, arXiv:2102.03432, doi: 10.48550/arXiv.2102.03432
- Noda, H., & Done, C. 2018, MNRAS, 480, 3898, doi: 10.1093/mnras/sty2032
- Panda, S., Pozo Nuñez, F., Bañados, E., & Heidt, J. 2024, ApJL, 968, L16, doi: 10.3847/2041-8213/ad5014

- Panda, S., & Śniegowska, M. 2024, ApJS, 272, 13, doi: 10.3847/1538-4365/ad344f
- Paolillo, M., & Papadakis, I. 2025, arXiv e-prints, arXiv:2506.23899, doi: 10.48550/arXiv.2506.23899
- Peters, C. M., Richards, G. T., Myers, A. D., et al. 2015, ApJ, 811, 95, doi: 10.1088/0004-637X/811/2/95
- Peterson, B. M., Wanders, I., Horne, K., et al. 1998, PASP, 110, 660, doi: 10.1086/316177
- Petrecca, V., Papadakis, I. E., Paolillo, M., De Cicco, D., & Bauer, F. E. 2024, A&A, 686, A286, doi: 10.1051/0004-6361/202449161
- Phan, D., Pradhan, N., & Jankowiak, M. 2019, arXiv preprint arXiv:1912.11554
- Pooley, D., Blackburne, J. A., Rappaport, S., & Schechter,P. L. 2007, ApJ, 661, 19, doi: 10.1086/512115
- Press, W. H., Rybicki, G. B., & Hewitt, J. N. 1992, ApJ, 385, 404, doi: 10.1086/170951
- Raiteri, C. M., Villata, M., Carosati, D., et al. 2021a, MNRAS, 501, 1100, doi: 10.1093/mnras/staa3561
- Raiteri, C. M., Villata, M., Larionov, V. M., et al. 2021b, MNRAS, 504, 5629, doi: 10.1093/mnras/stab1268
- Rasmussen, C. E., & Williams, C. K. I. 2006, Gaussian Processes for Machine Learning
- Ricci, C., & Trakhtenbrot, B. 2023, Nature Astronomy, 7, 1282, doi: 10.1038/s41550-023-02108-4
- Richards, G. T., Fan, X., Schneider, D. P., et al. 2001, AJ, 121, 2308, doi: 10.1086/320392
- Richards, G. T., Strauss, M. A., Fan, X., et al. 2006, AJ, 131, 2766, doi: 10.1086/503559
- Roux, A. 2002, PhD thesis, University of Pretoria, Pretoria
 Ruan, J. J., Anderson, S. F., Cales, S. L., et al. 2016, ApJ, 826, 188, doi: 10.3847/0004-637X/826/2/188
- Sánchez-Sáez, P., Lira, P., Mejía-Restrepo, J., et al. 2018, ApJ, 864, 87, doi: 10.3847/1538-4357/aad7f9
- Sánchez-Sáez, P., Reyes, I., Valenzuela, C., et al. 2021, AJ, 161, 141, doi: 10.3847/1538-3881/abd5c1
- Sánchez-Sáez, P., Arredondo, J., Bayo, A., et al. 2023, A&A, 675, A195, doi: 10.1051/0004-6361/202346077
- Savić, Đ. V., Jankov, I., Yu, W., et al. 2023, ApJ, 953, 138, doi: 10.3847/1538-4357/ace31a
- Schmidt, K. B., Rix, H.-W., Shields, J. C., et al. 2012, ApJ, 744, 147, doi: 10.1088/0004-637X/744/2/147
- Secunda, A., Greene, J. E., Jiang, Y.-F., Yao, P. Z., & Zoghbi, A. 2023, ApJ, 956, 81, doi: 10.3847/1538-4357/ace7d2
- Sergeev, S. G., Doroshenko, V. T., Golubinskiy, Yu. V., Merkulova, N. I., & Sergeeva, E. A. 2005, ApJ, 622, 129, doi: 10.1086/427820
- Sesar, B., Ivezic, Z., Lupton, R. H., et al. 2007, AJ, 134, 2236, doi: 10.1086/521819

- Shakura, N. I., & Sunyaev, R. A. 1973, A&A, 24, 337
- Smith, K. L., Mushotzky, R. F., Boyd, P. T., et al. 2018, ApJ, 857, 141, doi: 10.3847/1538-4357/aab88d
- Starkey, D. A., Horne, K., & Villforth, C. 2016, MNRAS, 456, 1960, doi: 10.1093/mnras/stv2744
- Stone, Z., Shen, Y., Burke, C. J., et al. 2022, MNRAS, 514, 164, doi: 10.1093/mnras/stac1259
- Suberlak, K. L., Ivezić, Ž., & MacLeod, C. 2021, ApJ, 907, 96, doi: 10.3847/1538-4357/abc698
- Temple, M. J., Hewett, P. C., & Banerji, M. 2021, MNRAS, 508, 737, doi: 10.1093/mnras/stab2586
- The Astropy Collaboration, Price-Whelan, A. M., Sipőcz, B. M., et al. 2018, AJ, 156, 123, doi: 10.3847/1538-3881/aabc4f
- The Astropy Collaboration, A., Robitaille, T. P., Tollerud, E. J., et al. 2013, A&A, 558, doi: 10.1051/0004-6361/201322068
- Uttley, P., & McHardy, I. M. 2001, MNRAS, 323, L26, doi: 10.1046/j.1365-8711.2001.04496.x
- Vanden Berk, D. E., Wilhite, B. C., Kron, R. G., et al. 2004, ApJ, 601, 692, doi: 10.1086/380563
- Vaughan, S., Edelson, R., Warwick, R. S., & Uttley, P. 2003, MNRAS, 345, 1271, doi: 10.1046/j.1365-2966.2003.07042.x
- Vehtari, A., Gelman, A., Simpson, D., Carpenter, B., & Bürkner, P.-C. 2021, Bayesian Analysis, 16, 667, doi: 10.1214/20-BA1221
- Villar, V. A., Cranmer, M., Berger, E., et al. 2021, ApJS, 255, 24, doi: 10.3847/1538-4365/ac0893
- Virtanen, P., Gommers, R., Oliphant, T. E., et al. 2020, NatMe, 17, 261, doi: 10.1038/s41592-019-0686-2
- Wang, Z. F., Burke, C. J., Liu, X., & Shen, Y. 2023, MNRAS, 521, 99, doi: 10.1093/mnras/stad532

- Ward, C., Gezari, S., Nugent, P., et al. 2022, ApJ, 936, 104, doi: 10.3847/1538-4357/ac8666
- Wilkins, D. R. 2019, MNRAS, 489, 1957, doi: 10.1093/mnras/stz2269
- York, D. G., Adelman, J., Anderson, J. E., et al. 2000, AJ, 120, 1579, doi: 10.1086/301513
- Yu, W., & Burke, C. 2025, EzTaoX: AGN light curve modeling with Gauassian Process, 0.1, Zenodo, doi: 10.5281/ZENODO.17467663
- Yu, W., & Richards, G. T. 2022, Astrophysics Source Code Library, ascl:2201.001
- Yu, W., Richards, G. T., Ruan, J. J., et al. 2025, arXiv e-prints, arXiv:2508.12076, doi: 10.48550/arXiv.2508.12076
- Yu, W., Richards, G. T., Vogeley, M. S., Moreno, J., & Graham, M. J. 2022, ApJ, 936, 132, doi: 10.3847/1538-4357/ac8351
- Yu, Z., Kochanek, C. S., Peterson, B. M., et al. 2020a, MNRAS, 491, 6045, doi: 10.1093/mnras/stz3464
- Yu, Z., Martini, P., Davis, T. M., et al. 2020b, ApJS, 246, 16, doi: 10.3847/1538-4365/ab5e7a
- Zhang, H., Yan, D., & Zhang, L. 2023, ApJ, 944, 103, doi: 10.3847/1538-4357/acafe5
- ZTF Team. 2025, ZTF Lightcurves, IPAC, doi: 10.26131/IRSA598
- Zu, Y., Kochanek, C. S., Kozłowski, S., & Udalski, A. 2013, ApJ, 765, 106, doi: 10.1088/0004-637X/765/2/106
- Zu, Y., Kochanek, C. S., & Peterson, B. M. 2011, ApJ, 735, 80, doi: 10.1088/0004-637X/735/2/80

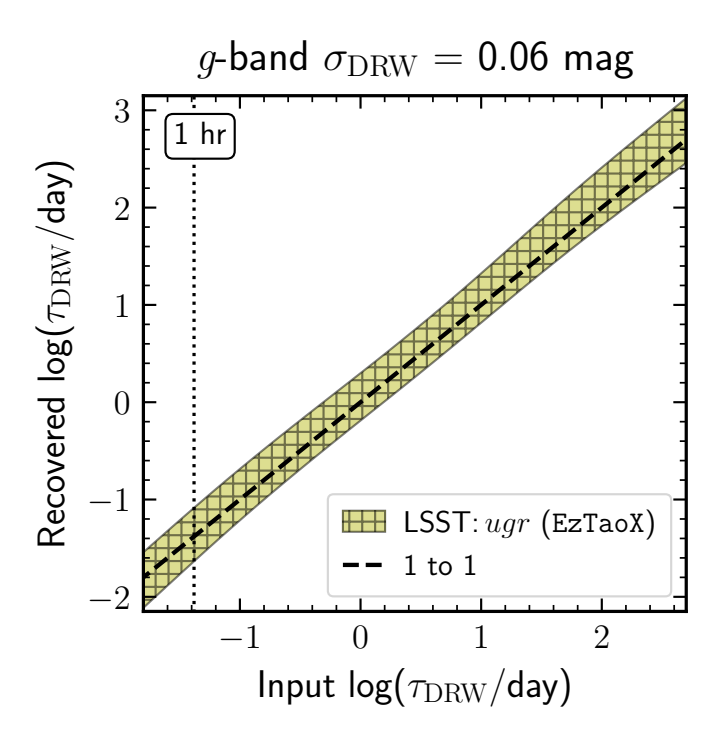


Figure 12. Recovered versus input τ_{DRW} from multiband (u, g, and r) light curves with EZTaoX. The 3 year LSST WFD g-band light curves are simulated with $\tau_{\text{DRW}} = 100$ days and $\sigma_{\text{DRW}} = 0.06$ mag (half the amplitude of the light curves in Figure 3). Even when the intrinsic σ_{DRW} is only a few times the photometric uncertainty, EZTaoX robustly recovers the input τ_{DRW} down to one hour.

APPENDIX

A. ADDITIONAL EZTaoX EXPERIMENTS

We perform additional experiments to demonstrate the robustness of EzTaoX in recovering DRW parameter under different regimes. To test its performance in recovering $\tau_{\rm DRW}$ at lower intrinsic variability amplitudes, we simulate a set of light curves similar to those in Section 3.1.3, but with the g-band $\sigma_{\rm DRW}$ reduced to 0.06 mag—half the value adopted in Section 3.1.3 and only about four times the average photometric uncertainty. As shown in Figure 12, EzTaoX still robustly recovers $\tau_{\rm DRW}$ down to one hour with 3 years of LSST WFD light curves. To evaluate its performance in recovering $\sigma_{\rm DRW}$ given larger intrinsic $\tau_{\rm DRW}$, we simulate another set of light curves similar to those in Section 3.1.4, but with the g-band $\tau_{\rm DRW}$ increased to 200 days—twice the value adopted in Section 3.1.4. As shown in Figure 13, EzTaoX continues to provide unbiased estimates of $\sigma_{\rm DRW}$ across the full simulated range.

B. ADDITIONAL JAVELIN EXPERIMENTS

The distribution of DRW parameters recovered by JAVELIN's multiband fitting depends on the properties of the light curves (e.g., cadence and mean photometric uncertainty) used in its initial fitting step, where a prior distribution of τ_{DRW} and σ_{DRW} is generated from a selected single-band light curve. To illustrate this sensitivity, we refit the light curves from Section 3.1.3 and Section 3.1.4, generating the prior distributions from the u- and g-band light curves. Figures 14 and 15 show the resulting distributions of τ_{DRW} and σ_{DRW} recoveries, highlighting that the final DRW parameter distributions differ depending on the band used to generate the priors. Moreover, more than 40% of JAVELIN fits fail the cleaning cuts when the u-band is used to generate the priors. This likely arises because the u-band has the poorest temporal sampling and highest photometric uncertainty, making the priors from JAVELIN's first fitting step unreliable.

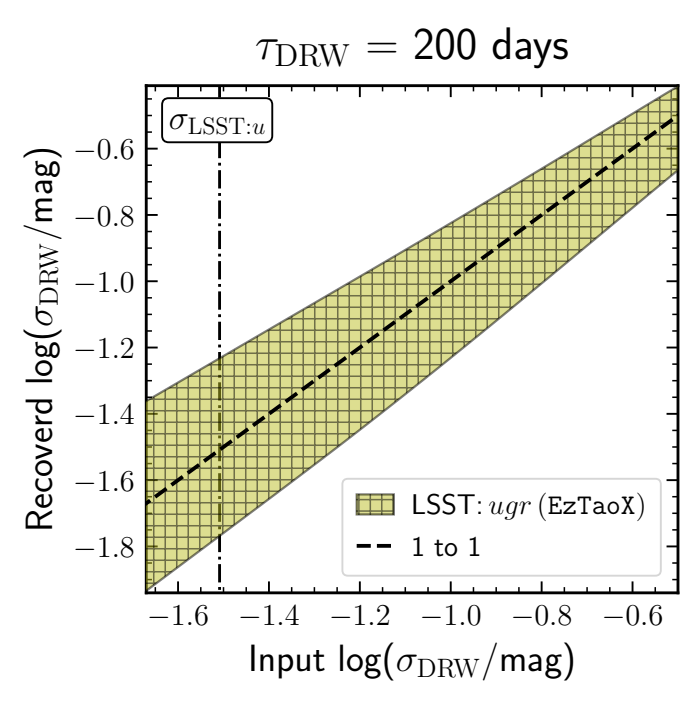


Figure 13. Recovered versus input σ_{DRW} from multiband (u, g, and r) light curves with EzTaoX. The 3 year LSST WFD g-band light curves are simulated with $\tau_{\text{DRW}} = 200$ days and $\sigma_{\text{DRW}} = 0.112$ mag. Consistent with Figure 5, EzTaoX yields unbiased estimates of σ_{DRW} across the full simulated range.

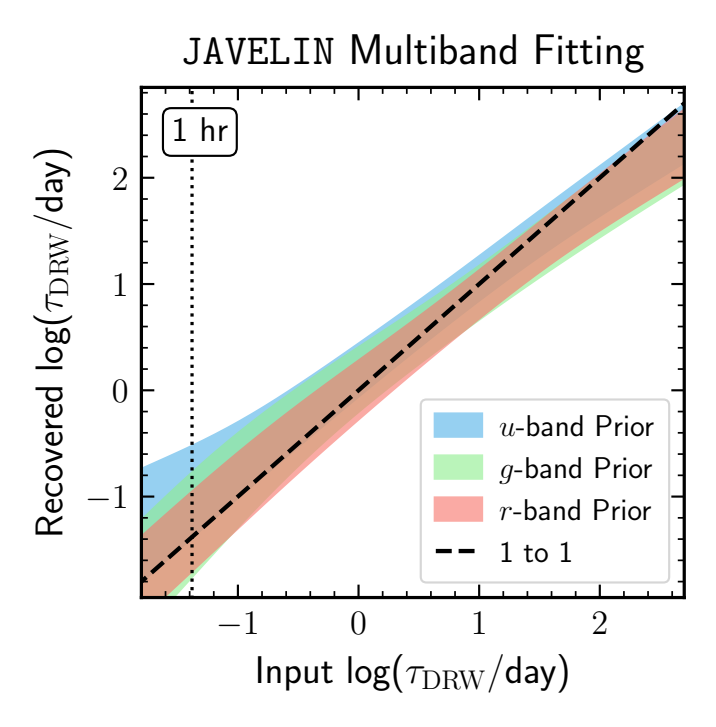


Figure 14. Recovered versus input τ_{DRW} from multiband (u, g, and r) light curves with JAVELIN. The blue, green, and red regions show the central 68% intervals for the distributions of the recovered τ_{DRW} with the priors derived from u-, g-, and r-band light curves, respectively. The recovered τ_{DRW} distributions differ depending on the band used to generate the priors.

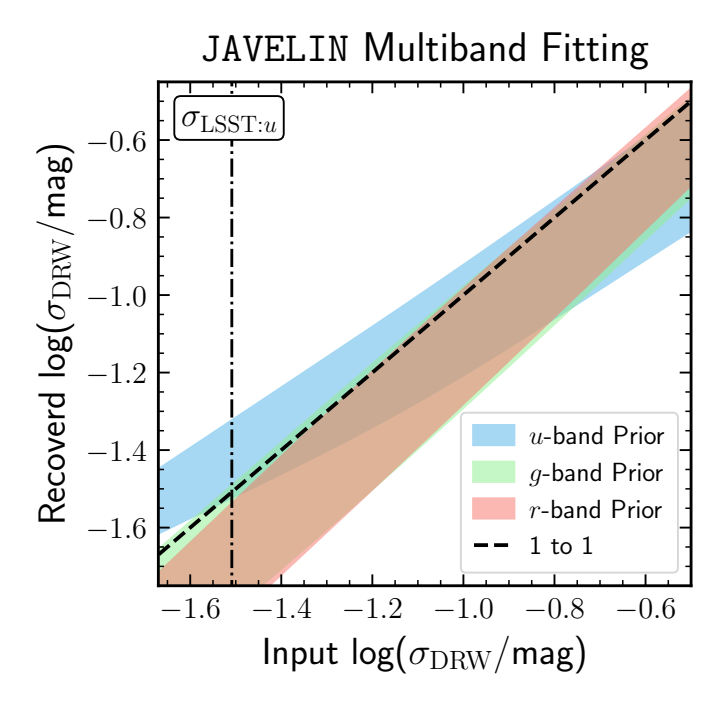


Figure 15. Recovered versus input σ_{DRW} from multiband (u, g, and r) light curves with JAVELIN. The blue, green, and red regions show the central 68% intervals for the distributions of the recovered σ_{DRW} with the priors derived from u-, g-, and r-band light curves, respectively. The recovered σ_{DRW} distributions differ depending on the band used to generate the priors.